Mapping of the surface profile of an asymmetric dielectric microcavity and identification of shape-sensitive internal modes

비대칭 유전체 미소 공진기의 경계형태 측정 및 형태에 민감한 내부 모드 분석

지도교수 안 경 원

이 논문을 이학박사 학위 논문으로 제출함

2013년 10월

서울대학교 대학원

물리 · 천문 학부

문 송 기

문송기의 박사학위논문을 인준함

2013년 12월

위 원 장	박 건 식	(인)
부 위 원 장	안 경 원	(인)
위 원	제 원 호	(인)
위 원	정 현 석	(인)
위 원	양 주 희	(인)

Mapping of the surface profile of an asymmetric dielectric microcavity and identification of shape-sensitive internal modes

by

Songky Moon

A Dissertation Submitted in Partial Fulfillment of the Requirements for the Degree of

Doctor of Philosophy
(Physics and Astronomy)
at the
Seoul National University

Abstract

In this thesis, I first present a non-destructive and non-contact high-resolution optical technique for profiling soft or fluidic boundary of an opaque object. This technique utilizes the fact that the angle width, the angular separation between two adjacent intensity minima in the forward shadow diffraction, is inversely proportional to the projected width of the object in the same direction. An analytic formula for reconstructing the boundary shape is obtained for an object with two-fold symmetry in terms of the angle widths measured for various rotational angles of the object. The typical error in determining the object shape parameter is less than 0.2%, which corresponds to 20 nm of radial accuracy when applied to an object with a mean radius of 10 μm.

I then apply the profiling technique to asymmetric liquid micro jet cavity and determine its surface profile in the accuracy enough to analyze the experimental results with theoretical concepts based on the one-to-one comparison between the experiments and with the numerical simulations. I found that the most dominant oscillation mode of our jet is the combination of quadrupolar and octapolar waves. The amplitudes of these two components are related by a certain quadratic relation, $\eta_2 \simeq B{\eta_1}^2$ (η_1 and η_2 are amplitudes of quadrupolar and octapolar oscillation, respectively). The coefficient B is obtained as 0.42 ± 0.08. I also survey the surface vibration of a microjet analytically by modifying Niels Bohr's non-linear hydrodynamical

treatment of the same problem, and find out that the expected value of B from this theory is nearly 0.41. The measured result and the theoretical prediction agree experimental error.

With this information, fundamental intra quasi-mode positions can be predicted by simulation within experimental error. Moreover, I also confirm that numerical simulations show good agreement with spectroscopic experimental results for non-trivial features of quasi-mode dynamics such as avoided crossing gaps.

Key Words : non-destructive measurement; surface oscillation; liquid jet; hydrodynamics; deformed microcavity; whispering gallery mode; quasi-mode interaction; fluorescence spectroscopy; shape-sensitive mode dynamics

Contents

List of Figures

List of Tables

Chapter 1

Introduction

Asymmetric optical microcavities [1, 2, 3] have drawn much attention from scientists and engineers for past two decades due to their distinctive advantages: good output directionality and relatively high quality (Q) factors. Directional output of the asymmetric optical microcavities are extensively studied in view of both its practical usefulness and implied manifestation of internal ray-dynamics [4, 5, 6, 7, 8, 9]. And high Q factors provide opportunities of spectroscopic analysis related to the advanced experimental studies for quantum chaos [3, 10, 11, 12], and applications such as biochemical sensors with hypersensitivity [13].

It has been one of the open problems for a long time in studies of asymmetric optical microcavities that a general discrepancy occurs between results from experiments and that of numerical simulations. Through extensive studies, it has been recognized that characteristics of the quasi-modes supported in these asymmetric microcavities depend sensitively on the exact shape of cavity boundary. For example, an elliptical cavity and a stadium-

shape cavity exhibit totally different quasi-mode characteristics although their shapes are quite similar [1, 2].

A quadrupolar-deformed microcavity (QDM), like a stadium-shape microcavity, is one of the nonintegrable systems where ray dynamics inside exhibit chaos. The chaos grows in general as the degree of deformation in a QDM is increased. However, a certain type of shape perturbation can delay the progress to chaos [5, 14]. A QDM that contains such perturbation can thus show a regular-system-like behavior, exhibiting quite different output directionality from that of a pure QDM even when the magnitude of perturbations is less than 1% of the radius.

These examples clearly indicate that, without knowledge of sufficiently accurate boundary profile, it is seriously limited to justify and analyze many observed optical phenomena theoretically. Conjecturing a certain boundary shape based on a few indirect evidences is hazardous. Many optical features of an asymmetric microcavity are now understood as manifestation of internal quasi-mode dynamics including complex mutual interactions [10, 11, 12]. Regarding only final outcomes hardly leads a proper interpretation. In this respect it can be said that accurate measure and detailed identification of internal quasi-mode dynamics become vital tasks to advance our understanding of asymmetric optical microcavities and their applications.

However, accurate measurement is sometimes even harder than the nuance that the terminology itself has. One important type of asymmetric optical microcavities is a two-dimensional liquid microjet cavity. A clear surface of liquid supports very high Q factor. And it has capability of changing its degree of deformation continuously [15], which is impossible for most

other microcavities made of solid. These two advantages make this type of cavity one of the most suitable systems for studying dynamical behaviors of cavity quasi-modes such as chaotic transition and tunneling mechanism [14, 11, 12]. But it is difficult to measure its surface boundary profile by using conventional high-resolution techniques, because of properties of the liquid jet. For example, the surface of liquid is non-Lambertian. i.e., the reflection from it is specular. Thus triangulation becomes inappropriate for this case. In order to accurately profile the boundary shape of these liquid microcavities, a new non-destructive imaging technique applicable to soft matter is strongly demanded.

In this thesis, I examine the boundary shape of the microjet cavity and the internal quasi-mode dynamics both theoretically and experimentally through following chapters. In chapter 2, the general aspects of the microjet cavity system is reviewed and the limit of the conventional approximated description of its boundary shape is addressed in the sense of spectroscopic experiment. Then I report the modified theoretical study to derive the magnitude of the surface oscillation which a microjet exhibits. This is a revision of Niels Bohr's one forgotten contribution to hydrodynamics [16]. In chapter 3, development of a new non-destructive and non-contact measurement technique suitable to the boundary profiling of a microjet is reported. This technique is based on the regularity of a forward diffraction pattern from an opaque and convex object, and provide 0.2% of the radius as the resolving power. In chapter 4, first I combine the results of two previous chapters. Realization of the measurement technique is shown, and by using it the revised boundary profile is verified. Next I examine the quasi-mode dynam-

ics for various experimental conditions and show that they match to that from the numerical calculation performed for the verified boundary profile. With this result, I suggest that the quasi-modes of the microjet cavity now can be theoretically identified. Chapter 5 contains a brief summary and conclusion.

Part of this thesis was published in the following papers:

1 Juhee Yang, Songky Moon, Sang-Bum Lee and Jai-Hyung Lee, Kyungwon An, "Development of a deformation-tunable quadrupolar microcavity", Rev. Sci. Instrum. 77, 083103 (2006).

2 Songky Moon, Juhee Yang, Sang-Bum Lee, Jeong-Bo Shim, Sang-Wook Kim, Jai-Hyung Lee, and Kyungwon An, "Nondestructive high-resolution soft-boundary profiling based on forward shadow diffraction", Optics Express 16, 11007 (2008).

Chapter 2

Surface oscillation and cavity boundary

2.1 Surface oscillation of a liquid column

The subject to be discussed in this chapter is one of non-trivial problems of science and engineering, but it is also related to very familiar phenomenon. A streaming liquid often shows regular surface modulation. We can notice it especially when we gaze a flow of liquid column poured from a non-circular orifice: for example, coffee from a pot, tea from a PET, water from a garden hose, and so on. See Fig. 2.1(a) and (b).

The terminology "non-circular" here might be seen as a misleading. For example, the neck of a PET is circular. However, we usually don't use the whole of it at a time. The liquid only pass through a part of the neck, *i.e.* non-circular orifice in reality.

Regarding the regularity, the modulation concerned here can be distinguished from an instability due to various external perturbations such as hand tremor or change of water pressure. This daily life situation is an intrinsic phenomenon governed by hydrodynamic principles with given initial conditions. And the fluidic modulation itself has been one of the basic problems in the field. The shape of the column as it advances, exhibiting the following characteristics. The pattern shown in this figure is stationary while the liquid moves in z direction. First, the cross-sectional shape of the jet in a plane perpendicular to the advancing direction varies periodically as we move along the stream. In particular, the directions of the major and minor axes are repeatedly exchanged, known as "axis switching" [17]. Second, the amplitude of surface oscillation decays and thus the cross-sectional shape gradually converges to a circle. Last, after a large distance, the jet column itself breaks into droplets.

Theoretically, this problem is often treated by approximating the surface oscillation to be described by a linear wave equation, mostly owing to Lord Rayleigh [18, 19] and Sir. Lamb [20]. The simple approach developed by them (from now on, I will simply note it to "linear theory" for convenience) gives reasonably good theoretical accounts for the aforementioned properties. Moreover, physical quantities calculated from the linear theory such as periods of oscillation and decay times are close enough to the observed values and thus it can be said that the linear theory is adequate for the most applications.

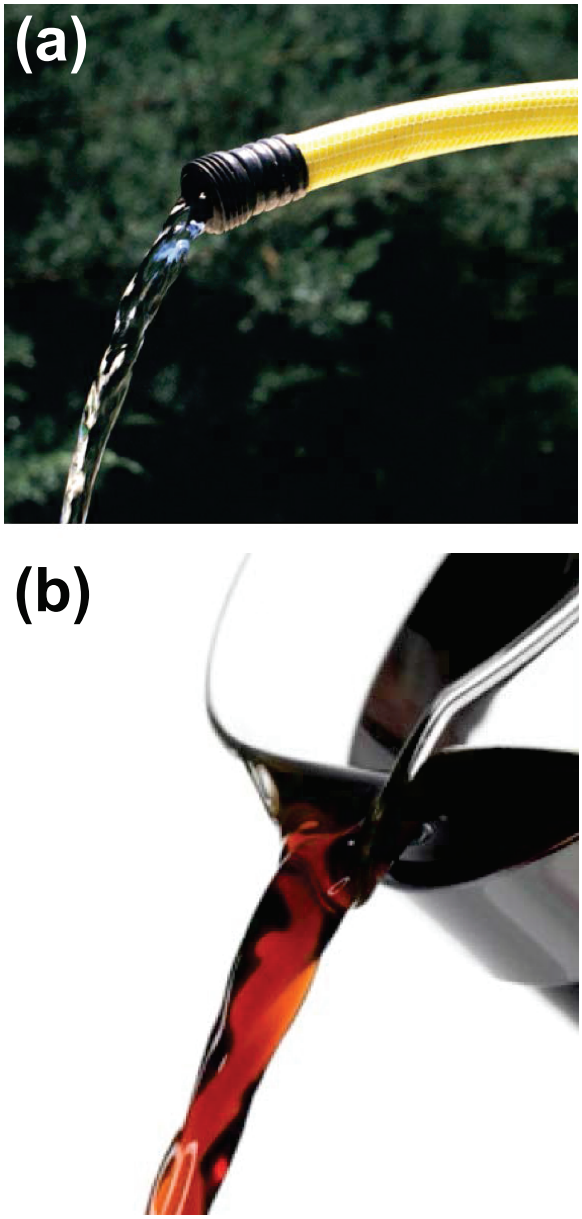

Figure 2.1: (a) Water from a garden hose. (b) Coffee poured from a pot.

However, "the most" is of course not "the all'. And sometime, even not "including every important aspects". As a fact the governing equations of motion of the situation contain non-linear interactions. Neglecting them inevitably limits the accuracy of analysis. So naturally when one is interested in some features sensitive to the details of the shape oscillation, the linear theory may not provide enough accuracy to account for the features of interest. As it will be discussed, the limitation seriously matters in regard of the aim of this study.

2.2 Deformation-tunable liquid microjet cavity

Before reviewing the linear theory and its limitations in more detail, here I introduce the core component of the experimental part of this study : a deformation-tunable liquid microjet cavity. Basically, the liquid jet is ejected vertically from the reservoir through a non-circular orifice by regulated pressure (within $\pm$0.005bar). The liquid is ethanol or water, or mixture of them. As the gain medium for lasing, dye material is doped. Fig. 2.2(a) shows a partial side view of the jet. The diameter of the horizontal section is about 25$\sim$35μm. Thus the mean radius is about 15 μm. The bright region of about 3 μm thickness is the segment excited by a pump laser beam. Fig. 2.2(b) is a 3-D model of a liquid jet.

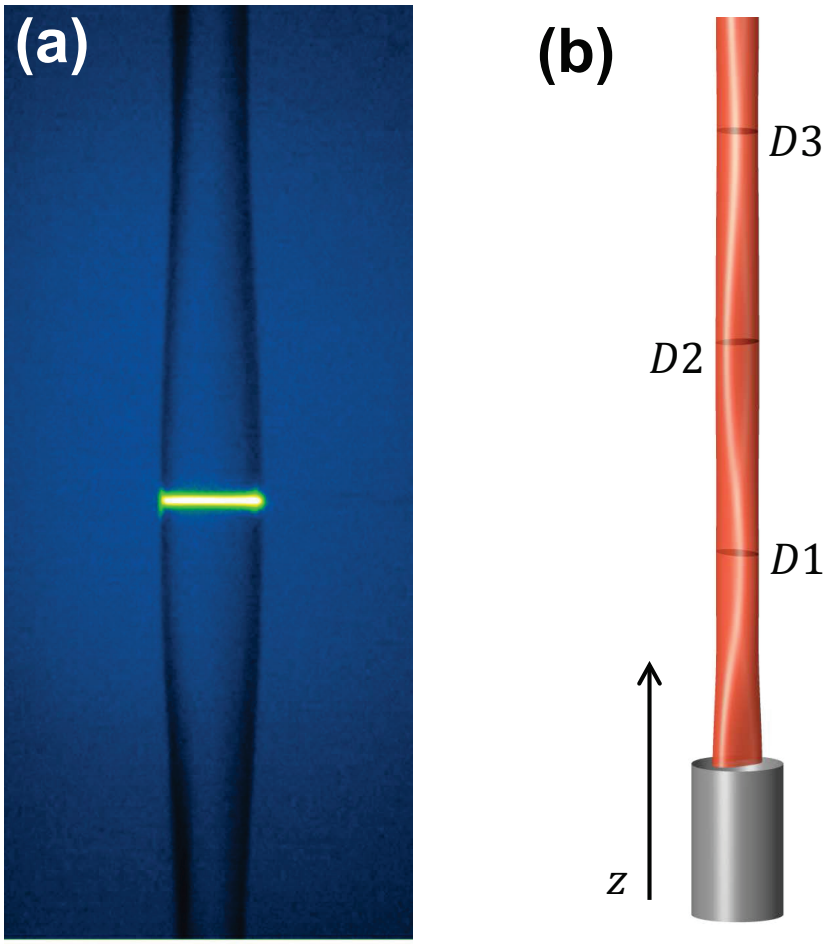

Figure 2.2: (a) Microscope image of the liquid jet column seen from the side. (b) A 3-D model of a liquid jet. D1, D2, and D3 are the extreme positions.

Fig. 2.3(a) shows the microscope image of the orifice. The shape of the orifice can be decomposed into multipolar(cos$n\theta$ in the $r-\theta$ plane) components as shown in Fig. 2.3(b). Choice of the origin is arbitrary. I take the center of mass of the orifice as the origin. Quadrupole (labeled by 2) and octapole (labeled by 4) are two most dominant ones. The decomposition serves as one of the initial conditions [21]. Another initial condition is the velocity at the bottom determined by the ejection pressure. From the microscope images of the jet such as Fig. 2.3(a), one can easily identify the major and minor axes until the amplitude of the surface oscillation becomes too small to be recognized. The two axes are perpendicular to each other. Moreover, the axis-switching is also clearly observed (The average period of the axis switching for Fig. 2.2(a) is 270 ± 10 μm).

The cross sections of the jet provide 2-dimensional deformed microcavities. To minimize the vertical curvature, only extreme positions (*i.e.* nodes or anti-nodes) are taken. Each of them are, from now on, named by its order from the bottom. For example, the nearest extreme position from the bottom is noted to D1. And the next is D2, ... and so on. This recognition is depicted in Fig. 2.2(b).

The degree of deformation can be varied with the ejection pressure [15]. It is one of the main novelty of the system. The background principle of this tunability is understood as an analogy of the harmonic oscillator. As shown in Fig. 2.4(a) due to the procedure of the fabrication (a Pasteur pipette is melted to be stuck, then asymmetrically pressed and cut) the tip of the

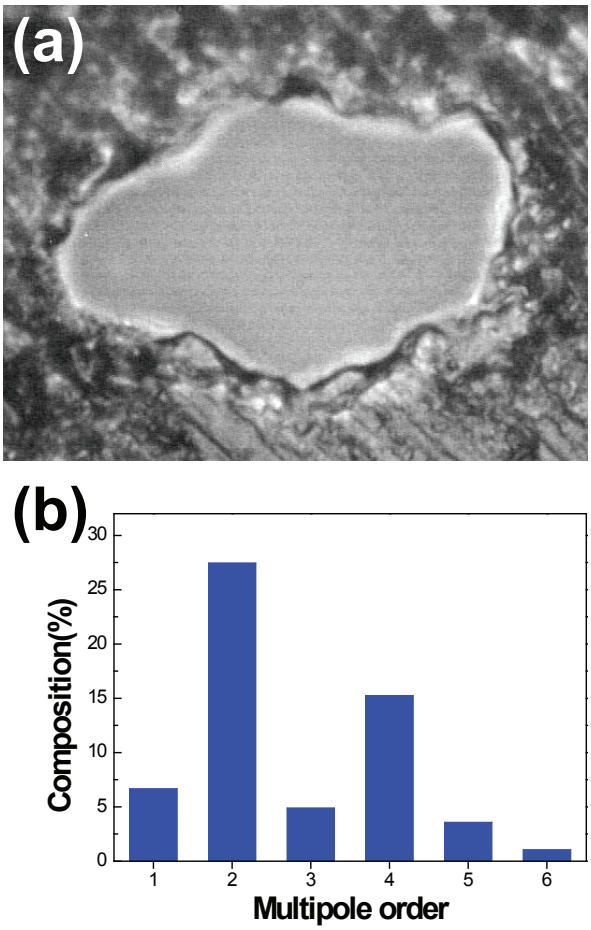

Figure 2.3: (a) Microscope image of the orifice. (b) Multipolar decomposition of the boundary profile of the orifice of (a).

liquid-ejection part have an internal inclination. Therefore phenomenologically the surface oscillation of the jet initially accompanies an overall radial velocity depends on the velocity of flow passes through the tip. A simple analogy for this situation depicted in Fig. 2.4(b). The harmonic oscillator (angular velocity ω of which initial displacement is A with non-zero initial velocity(v_0) the oscillation magnitude is $\sqrt{A^2 + (v_0/\omega)^2}$, not A.

Determining the boundary shape experimentally is a rather tricky task at this point. One can take microscope images alongside the major and minor axis, and evaluate the eccentricity ϵ at extreme positions as follow.

$$\epsilon(z) = \frac{L_{\mathrm{major}}(z) - L_{\mathrm{minor}}(z)}{L_{\mathrm{major}}(z) + L_{\mathrm{minor}}(z)}, \tag{2.1}$$

where $L_{\mathrm{major}}(z)$ and $L_{\mathrm{minor}}(z)$ are the lengths of the major and minor axes at a given height(z), respectively.

But mainly two problems arise. One, measurement accuracy of conventional microscope image of such a small and transparent object is limited, because of the resolving power and multiple reflection. If the resolution of the image is L_e, it approximately allows

$$\Delta\epsilon(z) = \pm 2L_e \frac{\sqrt{L_{\mathrm{major}}(z)^2 + L_{\mathrm{minor}}(z)^2}}{\left(L_{\mathrm{major}}(z) + L_{\mathrm{minor}}(z)\right)^2} \simeq \frac{\sqrt{2}L_e}{L_{\mathrm{major}}(z) + L_{\mathrm{minor}}(z)}, \tag{2.2}$$

as the range of error of $\epsilon(z)$. In the experiment, $L_{\mathrm{major}}(z) + L_{\mathrm{minor}}(z)$ is about 30μm. Thus even when L_e is about 200nm, $\epsilon(z)$ has the error range of ± 0.01, that is, about 10% of the typical magnitude of $\epsilon(z)$ (0.1$\sim$0.2).

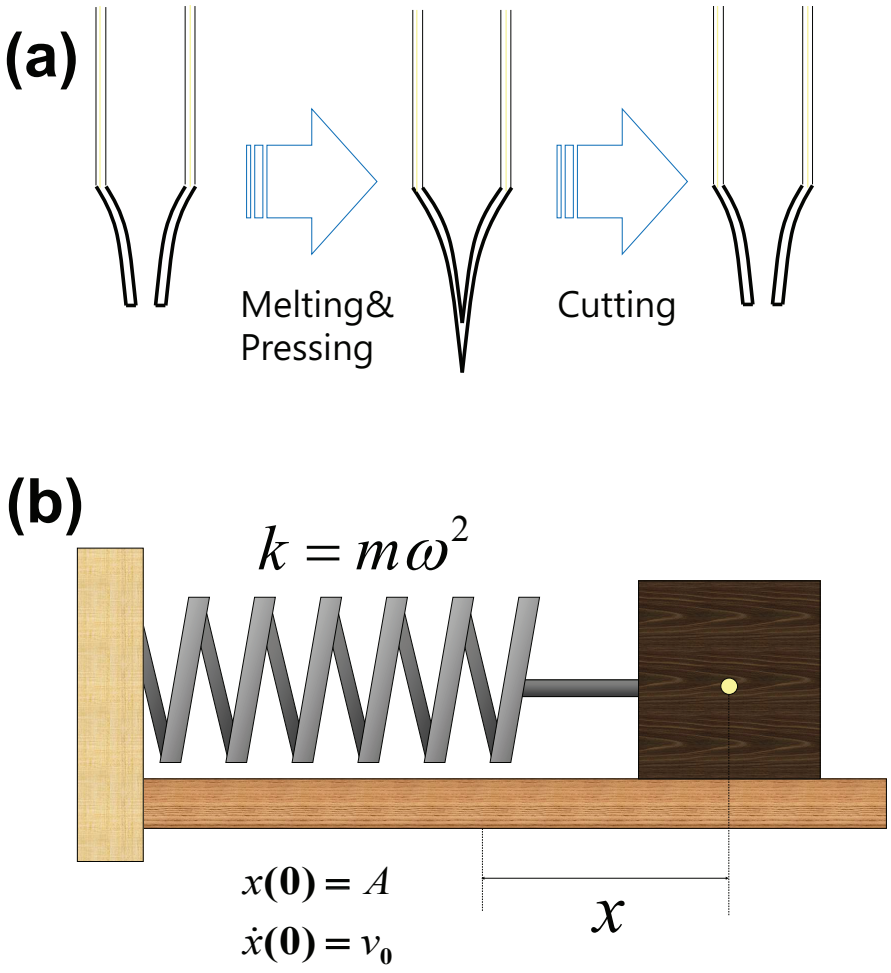

Figure 2.4: (a) Procedure to fabricate a tip of the ejection part (tip) of the microjet setup. (b) An analogy of the harmonic-oscillator with non-zero initial velocity.

Two, $\epsilon(z)$ is not enough information for the type of deformation alone. That is to say, there are infinitely many possible candidates of boundary shape for a certain $\epsilon(z)$. If one assumes that the shape is quadrupolar-deformed, in the next section it will be shown that this is the expectation of the linear theory, the shape can be determined quite accurately by taking the diffraction pattern from the jet and examining what the fitting parameter gives agreement between it and numerically simulated result. Naturally this is burdensome. And above all, without the guarantee that the deformation is really quadrupolar, the method is just a road to nowhere.

2.3 The linear theory of the surface oscillation of a liquid jet

2.3.1 The master equations

Following classical framework of theoretical hydrodynamics, we here treat the surface motion of a liquid jet by introducing the potential ϕ for the velocity $\mathbf{v}$, satisfying $\nabla\phi = \mathbf{v}$. Master equations of the motion are then written as follows in the cylindrical coordinates (r, θ, z):

$$\nabla^2\phi = 0, \tag{2.3}$$

$$\frac{T}{\rho a}\left(\frac{a}{R_1}+\frac{a}{R_2}\right)+\frac{1}{2}\left(\frac{\partial\phi}{\partial r}\right)^2+\frac{1}{2r^2}\left(\frac{\partial\phi}{\partial\theta}\right)^2+\frac{1}{2}\left(\frac{\partial\phi}{\partial z}\right)^2 = C, \tag{2.4}$$

$$\frac{\partial\phi}{\partial r}-\frac{1}{r^2}\frac{\partial\phi}{\partial\theta}\frac{\partial r}{\partial\theta}-\frac{\partial\phi}{\partial z}\frac{\partial r}{\partial z} = 0, \tag{2.5}$$

where a is the mean radius, T is the surface tension, ρ is the density of the jet material, C is a constant and R_1 and R_2 represent two principal radii of curvature of the jet surface. Equations (2.3)-(2.5) account for the irrationality of the fluid, the Bernoulli's principle and the condition for unbroken surface, respectively.

The sum of the reciprocals (principal curvatures κ_1 and κ_2) of the principal radii is just a trace of the shape operator:

$$\kappa_1 + \kappa_2 = \left[-r^3 \frac{\partial^2 r}{\partial z^2} + 2r \frac{\partial r}{\partial \theta} \frac{\partial r}{\partial z} \frac{\partial^2 r}{\partial \theta \partial z} - r \frac{\partial^2 r}{\partial \theta^2} \left(\frac{\partial r}{\partial z} \right)^2 - r \left(\frac{\partial r}{\partial \theta} \right)^2 \frac{\partial^2 r}{\partial z^2} \right.$$
$$\left. - r^2 \left(\frac{\partial r}{\partial z} \right)^2 + r^2 + 2 \left(\frac{\partial r}{\partial \theta} \right)^2 - r \frac{\partial^2 r}{\partial \theta^2} \right] \left[r^2 + \left(\frac{\partial r}{\partial \theta} \right)^2 + r^2 \left(\frac{\partial r}{\partial z} \right)^2 \right]^{-\frac{3}{2}}. \tag{2.6}$$

2.3.2 The linear theory : approximated master equations and their solution

The linear theory is based on simplifications of the above master equations. Namely, all the quadratic terms on Eq. (2.4) and Eq. (2.5) are to be neglected. These assumptions lead the following results.

$$\nabla^2 \phi' = 0, \tag{2.7}$$

$$\frac{T}{\rho a} - \frac{T}{\rho a^2} \left(\xi + \frac{\partial^2 \xi}{\partial \theta^2} \right) + v_z \frac{\partial \phi'}{\partial z} = 0, \tag{2.8}$$

$$\frac{\partial \phi'}{\partial r} - a v_z \frac{\partial \xi}{\partial z} = 0, \tag{2.9}$$

where

$$r = a + \xi(\theta, z), \tag{2.10}$$

$$\phi = v_z z + \phi'. \tag{2.11}$$

And the decay of the amplitude of the motion occurs due to the viscous damping. Then the solution ξ is expressed as a linear combination of the bases $\xi_n (n = 1, 2, 3, ...)$ given by

$$\xi_n = \cos n\theta \cos(k_n z + \chi_n) e^{-z/D_n}, \tag{2.12}$$

where $k_n \equiv 2\pi/\Lambda_n$ is the wave vector in z direction with Λ_n the oscillation wavelength, χ_n is the initial phase at the orifice and D_n is the decay length. Λ_n and D_n are obtained as following equations:

$$\Lambda_n/v_z = \frac{2\pi}{\sqrt{n(n^2-1)}}\sqrt{\frac{\rho a^3}{T}}, \tag{2.13}$$

$$D_n/v_z = \frac{1}{2n(n-1)}\frac{a^2}{\nu}, \tag{2.14}$$

ν is the kinematic viscosity of the liquid. The quantities Λ_n/v_z and D_n/v_z are the oscillation period and the decay time, respectively.

2.3.3 Application of the linear theory on the microjet cavity

Now let the result of the linear theory be applied to the liquid micro jet. For ethanol at 20.0°C , $T = 2.23 \times 10^{-2}$ N/m, $\rho = 789$ kg/m^3, and $\nu =$

1.52×10^{-6} m^2/s. Typically the jet is operated around $v_z \sim$10$\sim$20 m/s. Two most dominant components of the initial deformation is, as seen above, are quadrupole and octapole. With these values we obtain the period of quadrupolar oscillation $\Lambda_2/v_z = 28.0$ μs from Eq. (2.13). It agrees well with the observed value within the experimental error.

The decay time obtained from Eq. (2.14) is $D_2/v_z = 37.0$ μs. Comparing the quadrupolar and octapolar modes, we obtain $D_2/D_4 = 6$ and $\Lambda_2/\Lambda_4 = \sqrt{10}$. During one period of the quadrupolar oscillation, $\Lambda_2 = 300 \sim 600$ μm, the quadrupolar amplitude is halved whereas the octapolar amplitude decays by 2 orders of magnitude ($e^{-4.5} \sim 100$). Therefore, after 2 or 3 quadrupolar periods, the octapolar mode should become hardly noticeable according to the linear theory.

Based on these considerations, it can be expected that the cross-sectional shape of the jet at the extreme positions might be approximated as

$$r/a \simeq 1 + \eta(z) \cos 2\theta, \tag{2.15}$$

where $\eta(z)$ is identified as the eccentricity $\epsilon(z)$ at a certain height z. *i.e.* The deformation of a microcavities provided from the liquid microjet is quadrupole.

2.4 Failure of the linear theory : experimental evidences

2.4.1 Cavity boundary and cavity-modified fluorescence spectrum

Is this result in accord with the observed features? The most serious counterexample comes from spectroscopic experiments. Before discussing the details, let me first explain how those observations are made. As above mentioned, the liquid jet contains dye molecules which emit fluorescence when optically excited. When the small $z-$ segment of the jet column is excited by a pump laser as shown in Fig. 2.3(a), the fluorescence from dye molecules is modulated by the cavity resonances as shown in Fig. 2.5 (It is measured at D4 with jet-ejection pressure of 1.408 bar. The radius $a = 14 \pm 1$ μm and the room temperature is 19.5°C. The doping density of gain material - Rhodamine 590 dye - is 0.05mM/L. The cavity medium is ethanol with an index of refraction of 1.361 at 610nm-wavelength). The modulation comes about by the cavity quantum electrodynamics effect [23, 24].

Classically, the resonances in the cavity-modified fluorescence(CMF) spectrum are solutions of the Helmholtz equation with suitable boundary conditions for the system. In that sense they are simply denoted to "modes" on occasions [5, 25, 26]. However, they are not really eigen-modes because the system is dissipative. Instead, these type of eigen-solutions are traditionally called "quasi-(eigen)mode(state)s" [12, 24], terminology which I will use in this study from now on.

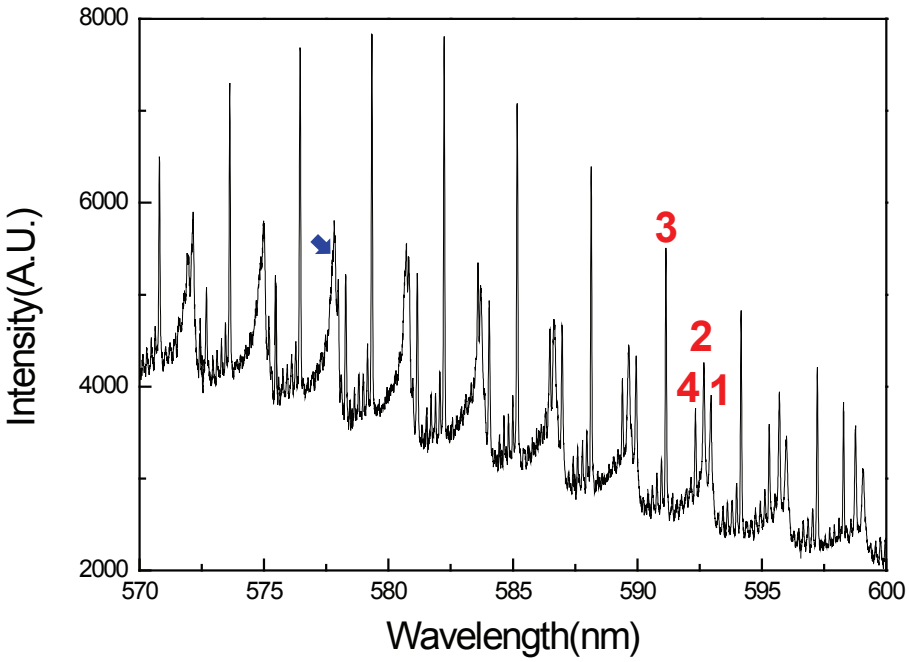

Figure 2.5: CMF spectrum from 570nm to 600nm. Experimental conditions are 1.408bar-D4-19.5°C-14 $\pm$ 1 μm.

It is noteworthy that in the CMF spectrum observed, locally similar (but not identical) packet-like structure is repeatedly appeared. Quasi-modes can be categorized into several groups by their behaviours through the evolution of the local structure [5, 24] . In Fig. 2.5, the repeating cycle is about 3nm and 5 groups of quasi-modes, with that each of them is labelled as $1 \ldots 5$ group respectively, are distinguished. Specifically, above 579nm locally similar structure consist of each member of 4 different resonance groups $(1, 2, 3, 4)$ is repeated. Red figures indicate the group numbers of each resonance between 590nm and 595nm. The group 5 begins to appear around 578nm (blue arrow) and visible below it. Summing up, one can find 5 resonance groups in this region. Details about the grouping and the labelling will be discussed in section 4.3. Additionally, the resonances exhibit considerably large Q factors. The group $1 : 10^5 \sim 10^6$, the group $2 : 10^4 \sim 10^5$, the group 3 : about 10^5, the group 4 : about 10^4, and the group 5 : about 10^3. The properties stated here are commonly observable in the CMF spectrum from the microjet cavity.

Since the boundary profile of the cavity is one of the boundary conditions determine the positions and the properties of the quasi-modes, we can then seek whether the given boundary profile leads corresponding theoretical results to the observed CMF spectrum in reverse with fixing other variables. To solve the Helmholtz equation for given boundary conditions numerically, I use the boundary element method [27]. Once the frequency and linewidth (or equivalently, the quality factor) of cavity resonances are obtained in this way, it is possible to compare them to the experimental data directly.

2.4.2 Results of the comparison

The result of the comparison is impressive. It turns out that the calculated cavity-resonances with the boundary profile Eq. (2.15) are strongly deviated from the actual ones in the spectrum. Even approximate matching is impossible, generally in the range of my investigation. Fig. 2.6(a) and Fig. 2.6(b) shows a dramatic example of the deviation. The format of both figures is noted to the "(quasi-)mode evolution diagram". It is developed to visualize the relative positions of quasi-modes in the packet-like structure that each of them belongs to, and the behaviours of the groups of quasi-modes. The reference positions are successively taken from a sequence of virtual quasi-modes with a regular free-spectral range (FSR).

Fig. 2.6(a) shows the experimentally observed positions of quasi-modes for the same conditions with that of Fig. 2.5. Eccentricity ϵ of this case is 0.19 ± 0.02. Fig. 2.6(b) displays the result from numerical calculation for $\epsilon = 0.19$. The positions of the quasi-modes are transformed into the relative size parameter, which will be defined in section 4.3. The horizontal axis (Reference X) represents the reference positions of the packets, while the vertical axis (X Gap) represents the relative positions of the quasi-modes to each reference.

As are clearly shown, the discrepancies are serious. In the experiment, it can be found that 5 distinguishable high-Q quasi-mode groups. However on the calculation-counterpart, we can only find 3 such groups. Moreover, experimentally observed groups interact with each other as one can see in the avoided crossings of their sequences, while not any crossing or avoided cross-

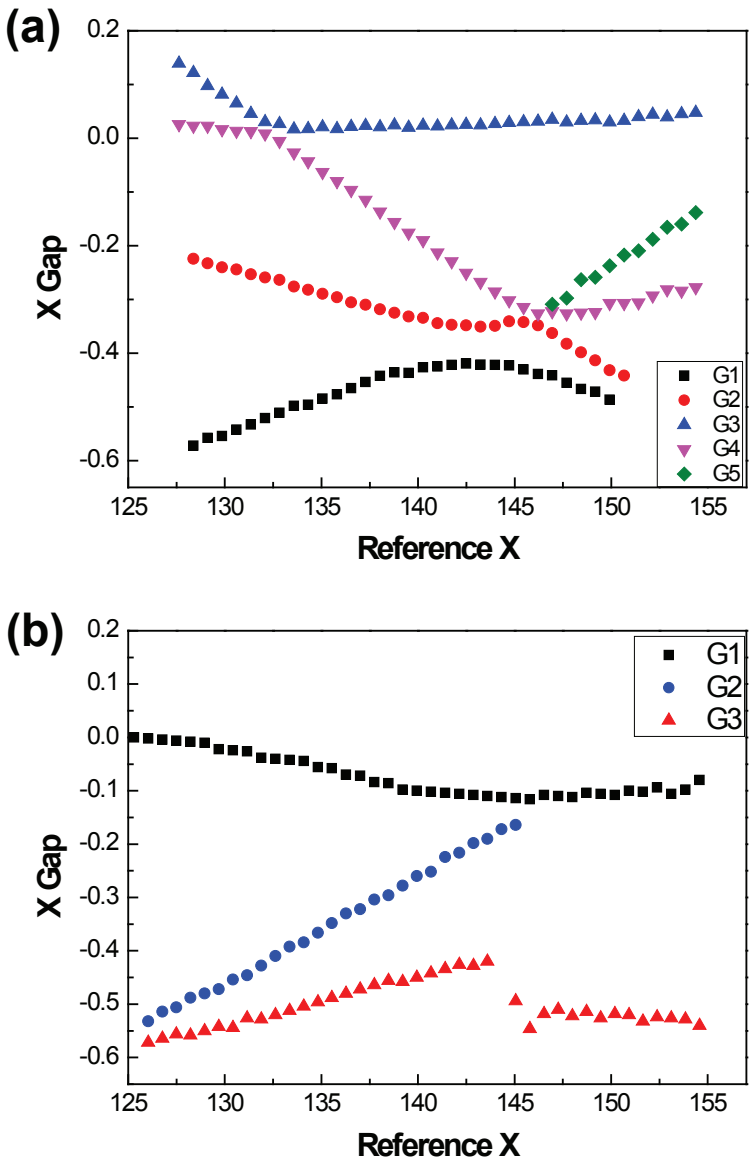

Figure 2.6: (a) Experimentally obtained quasi-mode evolution diagram when $\epsilon = 0.19 \pm 0.02$ (b) Theoretically obtained quasi-mode evolution diagram for the boundary of Eq. (2.15) with $\epsilon = 0.19$. **G** in legends denote 'quasi-mode group'.

ing structure does appear on the results from calculation within range of the investigation. Needless to say, the all positions of the quasi-modes from those two results generally deviate from each other. It might be supposed that the uncertainty of the eccentricity plays an important role to make the deviation. However, to see the continuous 5 high Q quasi-mode groups ϵ should be lowered below 0.14: It is out of the error bar. Moreover, even for that low eccentricity the detailed features of the quasi-mode evolution diagram are still different from the experimental result (See Appendix A).

Therefore one cannot but conclude that the quasi-mode dynamics as a whole is not predicted by the numerical simulation based on the boundary profile given by Eq. (2.15). That is to say, up to this point of ignorance of the boundary shape, simply we can not identify what the observed cavity quasi-mode is. As a consequence, physical interpretations are limited. This eclipses one of the important advantages of the system. Even though one can obtain spectroscopic data thanks to the high-Q factor supported by the asymmetric optical microcavity, the data is hard to be analyzed quantitatively, and a qualitative supposition can be hazardous.

2.4.3 Shape sensitivity of high-Q modes : A discussion on effect of a small perturbation in classical dynamics

What is then the actual cross-sectional shape of the jet? Considering the approximation nature of the linear theory and the fact that it can explain the overall features of the jet such as axis switching and oscillation period, we

expect that the quadrupolar component, the outcome of the linear theory, is still dominant in the actual boundary profile. There may then exist a small shape perturbation which is responsible for the weaker resonance mode interaction. One possible candidate for the perturbation is a small but persistent octapole component, considering the observed perpendicularity of the major and the minor axes and the shape symmetry of the liquid jet.

It is then instructive to consider particle motion in a classical wall (conventionally this kind of problem is denoted to the "billiard" problem) that is quadrupolar-deformed and in some other similiar-shaped walls with the same eccentricity. Such consideration is meaningful since it is a well-established fact that there exists a close connection between a classical trajectory and a wave solution for a given shape of the wall. It is known that non-regular boundary shapes such as quadrupole can induce chaotic dynamics and also result in resonance mode interactions. It is also known that even quite a small perturbation can change the particle dynamics significantly in a partially chaotic system. Considering the close connection between classical dynamics and wave solutions, we expect a small perturbation of a right type may explain the above discrepancy with the spectroscopic observations.

Let me illustrate the dramatic effects that can be induced by such a small perturbation. An ellipse is one of the shapes that manifest regular particle dynamics. It's boundary can be expressed in multipolar expansion as

$$r/a \simeq 1 + \eta \cos 2\theta + \frac{3}{4}\eta^2 \cos 4\theta + \frac{5}{8}\eta^3 \cos 6\theta \cdots \tag{2.16}$$

One can observe that the difference between the pure quadrupolar-deformed shape and the ellipse with the same eccentricity is quite small, amounting to at most 1/100 of the diameter $2a$ in the deformation range of $0 < \eta < 0.2$. Beyond $\eta = 0.2$, the convexity of quadrupole is broken like a peanut due to the contraction along the minor axis. However, internal particle dynamics in the elliptical or a semi-elliptical wall, whose profile is obtained by truncating the expansion in Eq. (2.16) beyond the second order of η, are quite different from those of the pure quadrupolar-deformed wall. It is because a small initial difference in particle trajectories can grow exponentially later on in the presence of chaos.

Classical particle dynamics is conveniently analyzed in Poincare surface of sections (PSOS), which is commonly used to visualize the particle motion in a 2-dimensional billiard. PSOS is a phase diagram which is drawn by reflection position (θ) and reflection angle (χ) of a particle upon bouncing off the boundary. Regular or quasi-periodic orbits are represented by concentration of dots around localized substructures such as islands or curves. Chaotic motion has no such concentration of dots, rather uniformly filling some regions called the chaotic sea in the phase space.

Figure 2.7 shows the PSOS of the pure quadrupole while Fig. 2.8 shows that of the ellipse, both drawn in terms of θ and $\sin\chi$ for $\epsilon = 0.16$. Almost the whole PSOS in Fig. 2.7 is chaotic while the PSOS in Fig. 2.8 consists of many periodic and quasi periodic orbits. Since it is practically impossible to fabricate a billiard with a perfectly elliptical or quadrupolar boundary, it is also meaningful to consider the PSOS of the truncated semi-ellipse for comparison as in Fig. 2.9. Though chaotic sea is present in considerable

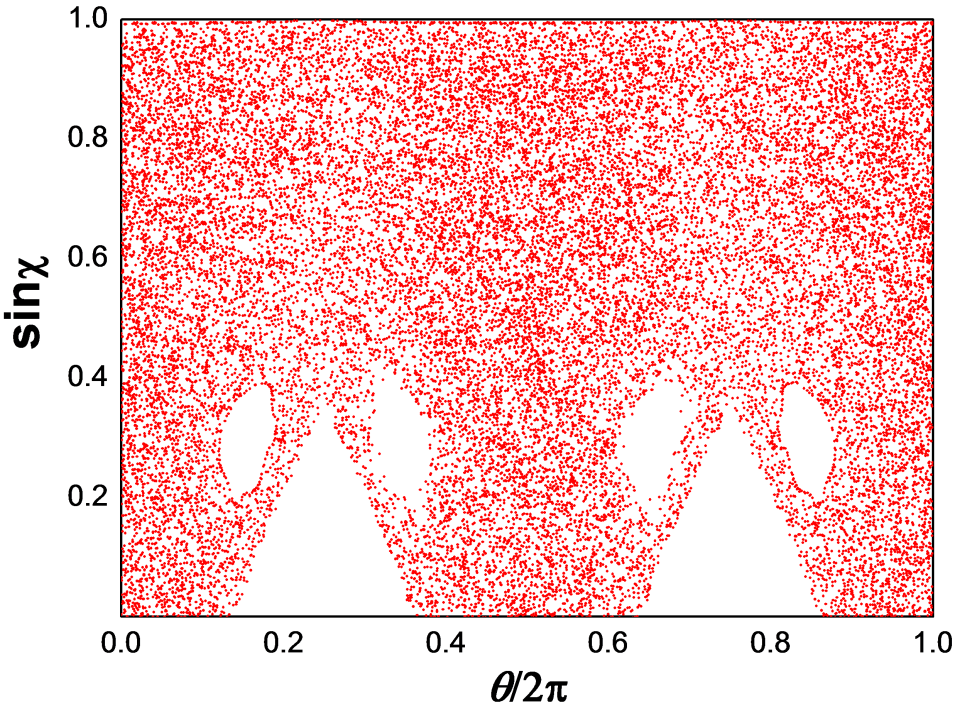

Figure 2.7: Poincare surface of sections for quadrupolar defromed billiard $r(\theta) = 1 + 0.16 \cos 2\theta$.

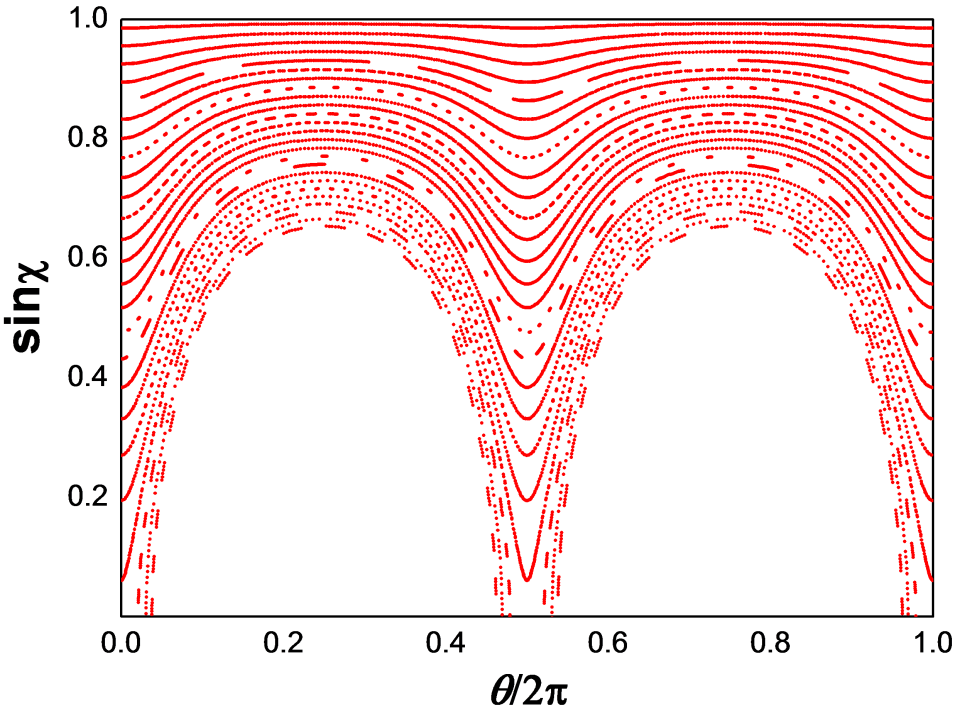

Figure 2.8: Poincare surface of sections for ellipse of which eccentricity $\epsilon = 0.16$.

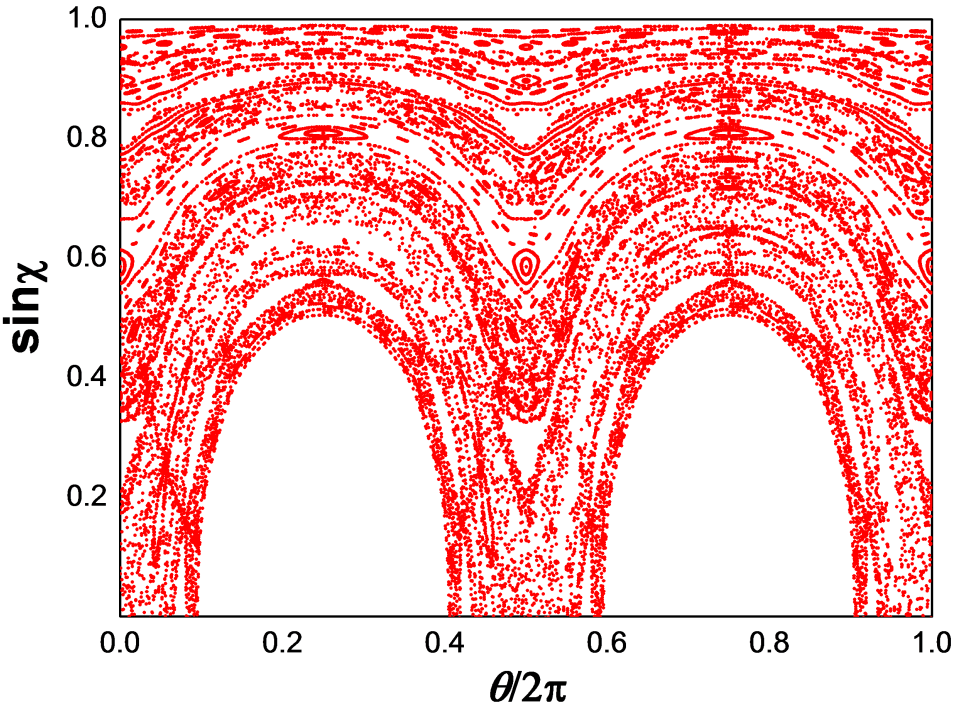

Figure 2.9: Poincare surface of sections for semi-ellipse with the eccentricity $\epsilon = 0.16$.

regions of the phase space, we still have curve-like or island-like structures corresponding to regular trajectories.

Interestingly, small differences in boundary profiles are often neglected in experiments with optical billiards, where ray motion corresponds to classical dynamics, though some reports have cautioned against such practice [29, 30], particularly when long-time dynamics becomes important. If experiments are performed with low-Q cavities, which is often the case with etched semiconductor microcavities, long-time dynamics hardly survive to affect the outcome, and thus one may neglect a small error in the boundary profile. If we deal with high-Q resonances, however, such as in dynamical tunneling and in mode evolution, long-time dynamics becomes important and thus a small difference in the boundary profile can lead to a big difference. By this reason, the spectroscopic observations of high-Q quasi-modes discussed in the preceding sections can constitute a very sensitive measure of the boundary shape of the 2-D optical billiard or the cross-sectional shape of our liquid jet.

2.5 Non-linear solution

2.5.1 Niels Bohr's modification

The following questions then naturally arise. What is the accurate profile of our liquid jet? How can we extend the hydrodynamic theory beyond the linear approximation to obtain the correct profile?

Here I introduce a work of another great scientist. In 1909, Niels Bohr at

the age of 23 before inventing the hydrogen model, considered the liquid jet problem including nonlinearity [16]. Conceiving the limitation of the linear approximation in the previous similar study [31], he modified the theory and derived an expression for the surface oscillation of a non-viscous liquid jet with a few lowest-order components. [28].

Since his intention was to measure the surface tension of the liquid by observing the surface oscillation, no further attention was paid to the boundary profile at extreme positions by himself. Since then, his work has been cited only related to surface tension, but other than that, the aspect of his work on the cross-sectional boundary profile has been completely unrecognized. When rewriting his result in terms of our notations, we obtain

$$\frac{r}{a} = 1 - \frac{1}{8}\eta^2 - \frac{1}{8}\eta^2 \cos 2k_z z + \eta \cos 2\theta \cos k_z z + \frac{1}{4}\eta^2 \cos 4\theta + \frac{1}{6}\eta^2 \cos 4\theta \cos 2k_z z, \tag{2.17}$$

where k_z is the wave vector in the propagation direction. Considering only nodal ($\cos k_z z = \cos 2k_z z = 1$) and anti-nodal ($\cos k_z z = -1, \cos 2k_z z = 1$) positions, and taking the major axis of the shape as the θ axis in the r-θ coordinates, Eq. (2.17) is simplified as

$$r/a = 1 - \frac{1}{4}\eta^2 + \eta \cos 2\theta + \frac{5}{12}\eta^2 \cos 4\theta. \tag{2.18}$$

The most noticeable feature in Bohr's analysis is that there exists a certain relation between the magnitude η_1 of the quadrupolar component and that of the octapolar one(note to η_1 and η_2, respectively).

$$\eta_2 = B{\eta_1}^2, \tag{2.19}$$

where B is a certain constant whose value is $0.41\dot{6} = 5/12$. (for a comparison, here I note that for an "semi ellipse" expressed by Eq. (2.16), similar relation holds and $B = 3/4$.) Let me allow some digression for explaining why I call this quantity 'B'. Originally, in my trace of the analysis summarized in this section it was one of two constants that represents newly introduced concepts in comparison with the solution of the linear theory : One, the area conservation [32], Two, correlation between quadrupole and octapole. Thus, at first I simply recognized them as 'A' and 'B', respectively. But eventually I realized that 'B' perfectly reminds the first letter of the name of the great scientist. So to honor his contribution to this subject, I decided to keep calling it 'B'.

Bohr's analysis is fascinating for its consideration of nonlinearity. But there are some limitations. In Bohr's analysis, the z-dependence is treated quite simply: the surface motion is regarded as a 2-dimensional oscillation and its time dependence is simply replaced by the z-dependence with an assumption that the fluid velocity is constant. This treatment is by no means rigorous due to the following reasons.

First, under gravity, the fluid velocity is not constant. Particularly, if the jet is ejected vertically upward like in our experimental setup, the velocity slows down. Second, the conservation of the flux dictates the velocity has to change periodically. The sectional area given by Eq. (2.18) is $\pi[1 + \frac{1}{4}\eta^2(1 - \cos 2kz)]$, having z dependence. Therefore, the velocity also has to change

as z in order keep the flux to be conserved.

If we limit ourselves to the region where the surface oscillations have not decayed sufficiently, *i.e.*, at several oscillation wavelengths away from the orifice, the change of velocity due to gravity is estimated to be negligibly small (less than 10^{-4} of the initial velocity). The velocity change due to the flux conservation, however, amounts to 1% of the initial velocity, in the same order of magnitude as the octapole component, if Bohr's result is believed, in the typical boundary profile. This is not small enough to be neglected, and its contribution to the boundary profile is uncertain at this point. Summing up these arguments, more rigorous analysis is needed to determine the boundary shape of the liquid jet. This is what I will discuss in the remains of this chapter.

2.5.2 Separation of the master equations by order of perturbation

We now back to Eq. (2.3)∼Eq. (2.6). The surface motion is decomposed by the orders of magnitude in η(up to the 2nd order) [33] :

$$r/a = F^{(0)} + \eta F^{(1)} + \frac{1}{2}\eta^2 F^{(2)}, \tag{2.20}$$

$$\phi = \phi^{(0)} + \eta\phi^{(1)} + \frac{1}{2}\eta^2\phi^{(2)}. \tag{2.21}$$

Then Eq. 2.6 becomes

$$\frac{a}{R_1}+\frac{a}{R_2}$$
$$= 1-\eta\left[F^{(1)}+\frac{\partial^2 F^{(1)}}{\partial\theta^2}+a^2\frac{\partial^2 F^{(1)}}{\partial z^2}\right]-\frac{1}{2}\eta^2\left[F^{(2)}+\frac{\partial^2 F^{(2)}}{\partial\theta^2}\right.$$
$$\left.-2(F^{(1)})^2-4F^{(1)}\frac{\partial^2 F^{(1)}}{\partial\theta^2}-\left(\frac{F^{(1)}}{\partial\theta}\right)^2+a^2\left(\frac{F^{(1)}}{\partial z}\right)^2+a^2\frac{\partial^2 F^{(2)}}{\partial z^2}\right]. \tag{2.22}$$

The zeroth motion corresponds to an upward-moving cylinder of a circular cross section. The gravitation causes the vertical velocity to decrease as the height: $v^2 = {v_z}^2 - 2gz$, where g is the gravitational acceleration and v_z is the initial velocity.

At the same time the radius has to increase to conserve the flux. Therefore, $F^{(0)}$ and $\phi^{(0)}$ are given by

$$F^{(0)} = 1+\frac{gz}{2{v_z}^2}, \tag{2.23}$$

$$\phi^{(0)} = \frac{gr^2}{4v_z}+v_z z-\frac{g}{2v_z}z^2. \tag{2.24}$$

The r-dependence of the velocity potential is required to satisfy the Laplace equation. Therefore, with these expressions substituted in Eq. (2.4), we can identify $C = T/(\rho a)+v_z^2/2-gz$. However, the terms containing g(the gravitational acceleration) are too small to make noticeable contribution. They will be thus neglected from now on.

2.5.3 The first order solution

The motion corresponding to the first-order terms is quite similar to the motion from the linear analysis. The master equations are:

$$\nabla^2\phi^{(1)} = 0, \tag{2.25}$$

$$-\frac{T}{\rho a}\left[F^{(1)} + \frac{\partial^2 F^{(1)}}{\partial\theta^2} + a^2\frac{\partial^2 F^{(1)}}{\partial z^2}\right] + v_z\frac{\partial\phi^{(1)}}{\partial z} = 0, \tag{2.26}$$

$$\frac{\partial\phi^{(1)}}{\partial r} - av_z\frac{\partial F^{(1)}}{\partial z} = 0. \tag{2.27}$$

A solution of the Laplace equation in the cylindrical coordinates can be written as a linear sum of Bessel's functions J_n. Therefore above equations are solved by substituting

$$\begin{aligned} F^{(1)} &= \cos n\theta \cos k_z z \\ \phi^{(1)} &= M_n J_n(ik_z r)\cos n\theta \sin k_z z \end{aligned} \tag{2.28}$$

where $n = 1, 2, 3, \ldots$ and M_n is a coefficient to be determined. Equations (2.26) and (2.27) then yield

$$M_n = -\frac{T}{\rho a k_z v_z J_n(ika)}(n^2 + k^2a^2 - 1) = \frac{iav_z}{J'_n(ika)}. \tag{2.29}$$

The factor $(k_z a)$ in the Bessel's function is noticeable. It is interpreted as an index number representing the ratio of the mean radius to the z-axial wavelength. A circular cylinder is the case when $ka \to 0$.

Equation (2.29) is further simplified when $k_z a \ll 1$. Using the approximated expression for the Bessel's function, the above relation can be approximated as

$$(ka)^2 = \frac{T}{\rho a^3 v_z^2} n(n^2-1)\left[1 + \frac{3n-1}{2n(n^2-1)}(k_z a)^2\right]. \tag{2.30}$$

or by solving for ka we get

$$ka \simeq \sqrt{n(n^2-1)}\left(\frac{T}{\rho a v_z^2}\right)^{1/2}\left[1 + \frac{3n-1}{4}\left(\frac{T}{\rho a v_z^2}\right)\right] \tag{2.31}$$

When the term proportional to $(k_z a)^2$ is negligible, the equation is reduced to the wave number formula derived in the linear analysis [Eq. (2.13)].

When $n = 1$ (dipolar motion), Eq. (2.31) is satisfied if and only if $k = 0$. The dipolar motion corresponds to a constant translation of the center of cross-sectional mass. It can be neglected as far as surface oscillation is concerned. Therefore, the quadrupolar ($n = 2$) motion is the lowest oscillatory motion.

2.5.4 The second order solution

Besides the Laplace equation, the second ordered equations are more complicated.

$$
\begin{aligned}
&-\frac{T}{\rho a}\left(F^{(2)}+\frac{\partial^2 F^{(2)}}{\partial\theta^2}+a^2\frac{\partial^2 F^{(2)}}{\partial z^2}\right)+v_z\frac{\partial\phi^{(2)}}{\partial z}\\
&+\frac{T}{\rho a}\left[-2\big(F^{(1)}\big)^2+\left(\frac{\partial F^{(1)}}{\partial\theta}\right)^2-4a^2F^{(1)}\frac{\partial^2 F^{(1)}}{\partial z^2}-a^2\left(\frac{\partial F^{(1)}}{\partial z}\right)^2\right]\\
&+\left(\frac{\partial\phi^{(1)}}{\partial r}\right)^2+\frac{1}{a^2}\left(\frac{\partial\phi^{(1)}}{\partial\theta}\right)^2+\left(\frac{\partial\phi^{(1)}}{\partial z}\right)^2\\
&+4v_zF^{(1)}\frac{\partial\phi^{(1)}}{\partial z}+2av_zF^{(1)}\frac{\partial^2\phi^{(1)}}{\partial z\partial r}=0,
\end{aligned}
\tag{2.32}
$$

$$
\begin{aligned}
\frac{\partial\phi^{(2)}}{\partial r}-av_z\frac{\partial F^{(2)}}{\partial z}+4F^{(1)}\frac{\partial\phi^{(1)}}{\partial r}-\frac{2}{a}\frac{\partial\phi^{(1)}}{\partial\theta}\frac{\partial F^{(1)}}{\partial\theta}-4av_zF^{(1)}\frac{\partial F^{(1)}}{\partial z}\\
-2a\frac{\partial\phi^{(1)}}{\partial z}\frac{\partial F^{(1)}}{\partial z}+2aF^{(1)}\frac{\partial^2\phi^{(1)}}{\partial r^2}=0.
\end{aligned}
\tag{2.33}
$$

By substituting the expressions in Eqs. (2.28) and (2.31) into $F^{(1)}$ and $\phi^{(1)}$, Eqs. (2.32) and (2.33) become

$$
\begin{aligned}
- & \left(F^{(2)} + \frac{\partial^2 F^{(2)}}{\partial\theta^2} + a^2\frac{\partial^2 F^{(2)}}{\partial z^2}\right) \\
+ & \frac{\rho a v_z}{T}\frac{\partial\phi^{(2)}}{\partial z} + \frac{\rho a}{T}a^2 k_z^2 {v_z}^2 \cos^2 n\theta \sin^2 k_z z \\
+ & \frac{T}{\rho a}\left[\frac{\left(n^2-1\right)^2}{{v_z}^2} + \frac{2(n^2-1)a^2k_z^2}{{v_z}^2}\right]\cos^2 n\theta\cos^2 k_z z \\
+ & \frac{T}{\rho a}\left[\frac{n^2\left(n^2-1\right)^2}{a^2k_z^2{v_z}^2} + \frac{2n^2(n^2-1)}{{v_z}^2} + \frac{n^2a^2k_z^2}{{v_z}^2}\right]\sin^2 n\theta\sin^2 k_z z \\
+ & \left[n^2\sin^2 n\theta\cos^2 kz - (2-4a^2k_z^2)\cos^2 n\theta\cos^2 kz - a^2k_z^2\cos^2 n\theta\sin^2 k_z z\right] \\
- & 4(n^2-1+a^2k_z^2)\cos^2 n\theta\cos^2 k_z z - \frac{2\rho a}{T}a^2k_z^2{v_z}^2\cos^2 n\theta\cos^2 k_z z = 0,
\end{aligned}
\tag{2.34}
$$

$$
\begin{aligned}
\frac{\partial\phi^{(2)}}{\partial r} - a v_z\frac{\partial F^{(2)}}{\partial z} + \frac{T}{\rho a}\frac{1}{a k_z v_z}n^2(n^2-1+a^2k_z^2)\sin^2 n\theta\sin 2k_z z \\
-\frac{T}{\rho a}\frac{a k_z}{v_z}n^2(n^2-1+a^2k_z^2)\cos^2 n\theta\sin 2k_z z = 0.
\end{aligned}
\tag{2.35}
$$

The terms comparable to or smaller than $a^4k_z^4T/(\rho a)$ have been neglected since the sum of them would contribute the final result by no more than 0.01%.

Now we are ready to evaluate the second ordered motion $F^{(2)}$. The velocity potential must satisfies both Laplace equation and Eq. (2.35). Therefore, $\phi^{(2)}$ and $F^{(2)}$ can be written as

$$
\begin{aligned}
\phi^{(2)} &= J_0(i2k_z r)\gamma_0(z) + J_{2n}(i2k_z r)\cos 2n\theta\gamma_{2n}(z), \\
F^{(2)} &= \delta_0(z) + \cos 2n\theta\delta_{2n}(z).
\end{aligned}
\tag{2.36}
$$

The function $\delta_0(z)$ is related to the area conservation. Carrying on the calculation further yields the expression for $\delta_{2n}(z)$.

$$\delta_{2n}(z) = \frac{2n^3+5n^2-2n-2}{4(4n^2-1)} + \frac{n^2+n+1}{4n(4n^2-1)}a^2k_z^2 + \left[\frac{-2n^3+7n^2+2n-4}{4(2n^2+1)} + \frac{-40n^5+22n^4+23n^3+17n^2+11n+1}{4n(2n+1)(2n^2+1)^2}a^2k_z^2\right]\cos 2k_z z. \tag{2.37}$$

Then, also a relation between the quadrupolar magnitude and the octapolar magnitude arises. Let the coefficient attached to $\eta^2\cos 4\theta$ be denoted to $B_{n=2}$. Its expression is then obtained from $\delta_4(z)$ with $n = 2$ (octapole component) and $\cos 2k_z z = 1$ (nodal and anti-nodal positions):

$$B_{n=2} = \frac{1}{2}\,\delta_4(z)|_{\cos 2k_z z=1} = \frac{5}{12} - \frac{232}{3240}a^2k_z^2 \simeq 0.417 - 0.07a^2k_z^2. \tag{2.38}$$

Let us focus on the lowest motion, $n = 2$. The term proportional to $(ak_z)^2$ is very small: $-0.07a^2k_z^2 \simeq 0.42T/\rho a{v_z}^2 \simeq 0.8\ [\mathrm{m}^2/\mathrm{s}^2]/({v_z}^2) \sim 10^{-3}$ considering that the velocity v_z is typically $10 \sim 20$ m/s. In Fig. 2.10 $B_{n=2}$ in the function of v_z is shown.

Comparing the final result Eq. (2.38) with Bohr's, now in the long run we can safely say that the magnitude of $B_{n=2}$ is quite similar to B at typical conditions of the microjet. Of course it may be an accident. But I checked

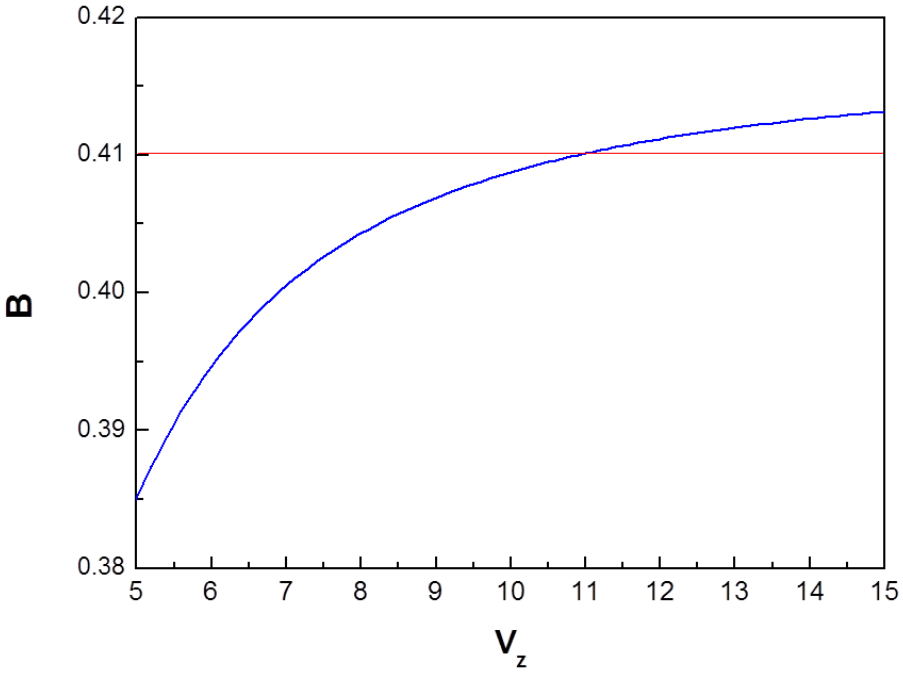

Figure 2.10: Blue curved line : $B_{n=2}$ in the function of v_z. Red horizontal line : a constant line at $B_{n=2} = 0.41$.

several cases of daily life situations which related to this problem and found that many of them lead similar operating conditions. For example, for a typical garden hose water shoot out has the velocity about $2 \sim 3$ m/s, and the radius of the stream about $1 \sim 2$ cm. Thus $(ak_z)^2$ is about $0.1 \sim 0.3$. Tap water from a faucet has $1 \sim 3$ m/s for its velocity and about 1 for the radius. Here $(ak_z)^2$ is roughly $0.1 \sim 0.2$.

Chapter 3

Development of surface mapping technique

3.1 A review of preceding studies

To test the surface profile derived in the previous section experimentally, a surface measurement technique which is applicable to the microjet and has very high resolution is needed. Considering the typical radius of the microjet ($a \sim 15\mu$m) and deformation ($\eta = 0.1 \sim 0.2$), the magnitude of $0.41a\eta^2$ is only about 40nm $\sim$250nm. The demanded technique should enable us to resolve this amount of perturbation. Unfortunately, it is hard to find among the conventional techniques that satisfy these two requirement simultaneously.

In science and technology it is often necessary to know boundary shapes of two- and three-dimensional microscopic objects such as biological cells [34, 35, 36], micro-organisms [37, 38], scatterers in suspension [39], opti-

cal fibers [40], metallic wires, micropillars and microcavities [29, 30, 41]. There exist several imaging techniques for profiling shapes of two- or three-dimensional object. Non-destructive and non-contact optical imaging techniques such as scanning microscopy in various forms can provide wavelength-order resolution in shape profiling. Although scanning electron microscopy, scanning tunneling microscopy, atomic force microscopy and their variations provide nanometer-resolution on local surface structures, they are of little use if one needs to know the overall geometrical shape of an entire object unless the object is cut so that its cross sectional shape of boundary can be profiled with these techniques. This approach still may work if the object is a solid. However, if the object is soft matter such as biological or fluidic objects, these intrusive techniques simply cannot be used.

In recent years, several groups have introduced imaging techniques based on phase measurement such as differential phase-contrast microscopy [34], optical coherent phase microscopy [35], Mach-Zender interferometer [36], scanning interferometric aperture-less microscopy [42], phase-shifting digital holography [43], fast Fourier phase microscopy [44], and so on.

However, these techniques, based on interferometry, are most effective for probing one-dimensional objects such as layered or planar structures [34, 47, 48] or profiling mildly curved surfaces such as mirror or lens surfaces [49, 50, 51] while some providing the Angstrom-order resolution [45]. For two or three dimensional objects, most of these techniques provide geometric accuracy only in the order of wavelength although overall features of the object can be well reconstructed.

In summary, it is hard to find an appropriate method for profiling a

fluidic-columnar object like the microjet. The difficulty becomes more serious due to its clear surface and the transparency. Surface of a fluid volume is non-Lambertian. Light incident on the surface undergoes reflection and transmission following Fresnel's equation. And the transmitted ray would contribute multiple internal reflection. Therefore for surface profiling of the microjet it is also hard to use the conventional triangulation method which is based on the assumption that for a fixed light source simply reflected ray from the target surface can be detected at an arbitrary position [52, 53].

In this section, I report a new surface profiling technique which is applicable to a fluidic and columnar object and has enough resolution. Main ideas of developing the new technique is to make use of phase-information to overcome the resolution limit, and to remove the transparency effectively to reduce the difficulty arisen from the multiple reflection [54].

3.2 Forward diffraction pattern by an opaque object

The first step is considering the diffraction pattern by a single slit of width d. For this textbook example, it is not well appreciated that the angular spacing between adjacent diffraction maxima/minima is inversely proportional to the projection width of the slit in the direction from the slit to the location of the maxima. This can be easily seen from the well known formula for the intensity distribution of the diffracted wave

$$I(\theta) \propto \left[\frac{\sin(\pi d \sin\theta/\lambda)}{\pi d \sin\theta/\lambda}\right]^2, \tag{3.1}$$

where the angle θ is measured from the forward direction normal to the plane of the slit. The angular spacing between adjacent peaks is then

$$\Delta\theta = \frac{\lambda}{d\cos\theta}, \tag{3.2}$$

where we recognize $d\cos\theta$ to be the projection width of the slit in the direction of θ. The same result holds for the diffraction pattern by an opaque strip by Babinet's complementary principle.

For another example, let us consider the diffraction pattern by an absorbing spherical cylinder. It is well known that the diffraction pattern by a transparent cylinder has somewhat irregular spacings between adjacent peaks, so as in Mie scattering. Obviously, the above result does not hold in this case. When the absorption is increased, however, so as to make the cylinder opaque, regular spacings emerge as shown in Fig. 3.1, the incident plane wave is attenuated (intensity wise) across the cylinder by a transmittance factor $T = \exp(-2n_r x/Q_{\text{abs}})$. Here Q_{abs} is defined as

$$Q_{\text{abs}} = \frac{n_r}{2n_i}, \tag{3.3}$$

where n_r and n_i are the real and imaginary parts of index of refraction of the cylinder medium and the size parameter x is defined as

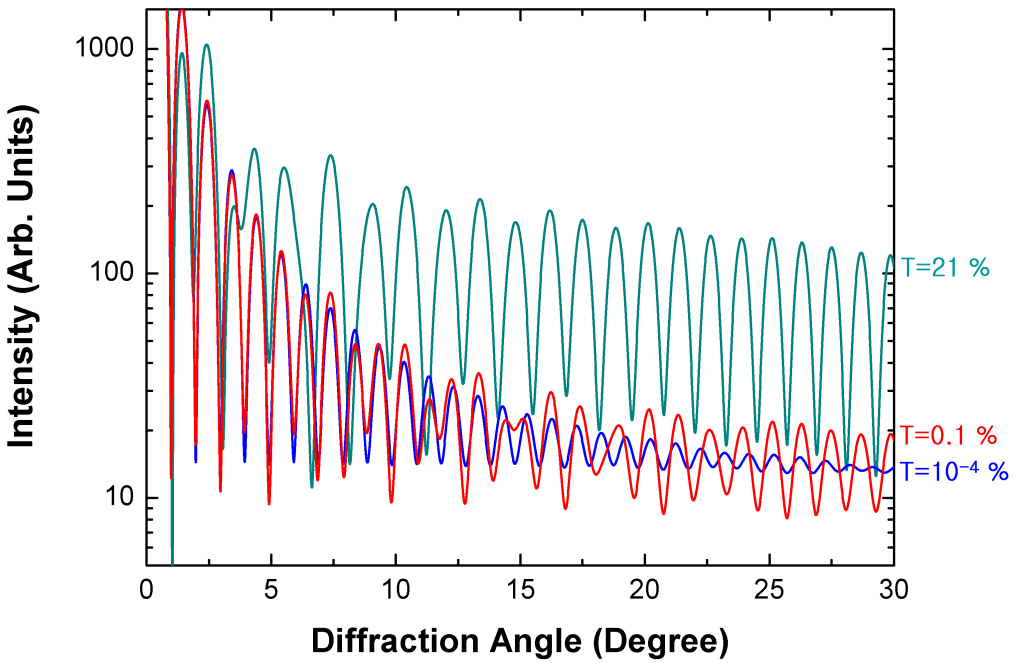

Figure 3.1: Diffraction patterns of an absorbing cylindrical object with the size parameter x=180. The real part of its index of refraction is 1.361 while its imaginary part is 0.0022 (T=21%, $Q_{\rm abs}$=310), 0.0096 (T=0.1%, $Q_{\rm abs}$=71) or 0.019 (T=10^{-4}%, $Q_{\rm abs}$=36).

$$x = \frac{2\pi a}{\lambda}, \tag{3.4}$$

with a the radius of the cylinder.

When the object is not opaque enough, not only diffraction but also wave refraction occur. In this case, the geometrical feature of the cylinder is encoded in a complicated way in a refracted wave, which is added to the diffracted wave, and results in irregularly spaced peaks. On the other hand, when the object is opaque, only the shadow diffraction occurs carrying the information on the projection width of the object. For the cylinder, the projection width is uniform, resulting in equally spaced peaks as shown in Fig. 3.1. It is instructive to note that irregularity still persist when T=0.1% ($Q_{\rm abs}$=71), whereas regularly spaced peaks are observed when T=10^{-4}% ($Q_{\rm abs}$=36), sufficiently satisfying the condition of effective opaqueness. A criterion can be set between $T = 0.1\%$ and $T = 10^{-4}\%$. I suggest $T = 0.001\%$. In the sense of optical density(OD= $-\ln T$), it corresponds 6.9. For $x = 180$ and $n_r = 1.361$, $n_i = 0.016$ is the guideline.

A natural question is then whether the results in the above two special cases can be extended to other opaque objects of arbitrary shape. The answer is yes and its proof is given in the next section.

3.3 Derivation of the forward shadow diffraction pattern by an opaque object

Next step is considering a plane electromagnetic wave of transverse-magnetic polarization incident on an opaque two-dimensional convex object which lies on the xy-plane as illustrated in Fig. 3.2. A plane electromagnetic wave with a wave vector $\mathbf{k_0}$ is incident on the object. The boundary of the object is described by $r(\phi)$ with ϕ the polar angle and $\hat{\mathbf{n}}$ the unit vector normal to the boundary. The polar angle is measured with respect to the direction of $\mathbf{k_0}$. The major axis of the object is rotated by β from the $\mathbf{k_0}$ direction. The region of the object specified by the condition $\phi_{b2} < \phi < \phi_{b1}$ is shadowed. The diffracted wave with a wave vector $\mathbf{k}$ in the direction of θ is considered.

Now the incident waves are written as $\mathbf{E}_i = \hat{\mathbf{z}} E_0 e^{i\mathbf{k}_0 \cdot \mathbf{x}}$ and $\mathbf{B}_i = (\mathbf{k}_0 \times \hat{\mathbf{z}} E_0/\omega) e^{i\mathbf{k}_0 \cdot \mathbf{x}}$, where $\hat{\mathbf{z}}$ is a unit vector in z direction, $\mathbf{k}_0$ is the wave vector in x direction with $|\mathbf{k}_0| = \omega/c = 2\pi/\lambda$ and $\mathbf{x}$ is a position vector in x-y plane.

Starting from the Kirchhoff integral, we can approximately describe the diffracted amplitude with the following equations [56].

$$\mathbf{E} \to \frac{i}{4\pi} \oint \left[\omega \hat{\mathbf{z}} \cdot (\hat{\mathbf{n}} \times \mathbf{B}_s) + \hat{\mathbf{z}} \cdot (\mathbf{k} \times (\hat{\mathbf{n}} \times \mathbf{E}_s)\right] e^{-i\mathbf{k} \cdot \mathbf{r}(\phi)} dl, \qquad (3.5)$$

where $\hat{\mathbf{n}}$ is a unit vector outward normal to the surface, $\mathbf{k}$ is the diffracted wave vector, $\mathbf{r}(\phi)$ is the position vector at polar angle ϕ lying on the boundary surface of the object and $\mathbf{E}_s$ and $\mathbf{B}_s$ are the scattered electric and mag-

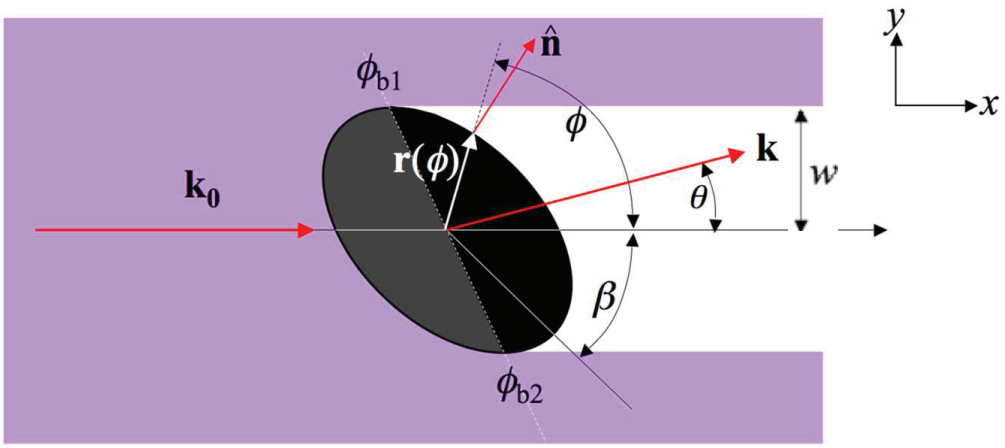

Figure 3.2: A graphical scheme of the shadow diffraction of an two dimensional convex object with twofold symmetry. $\mathbf{k_0}$ is the incident wave vector, and $\mathbf{k}$ is the diffracted wave vector.

netic fields at the boundary surface, subject to the boundary conditions to be discussed below.

Interest of this study lies in the short wavelength limit specified as $kr >> 1$. In this limit, the boundary surface is divided into two regions, a shadow region ($\hat{\mathbf{n}} \cdot \mathbf{k} > \mathbf{0}$) and an illuminated region ($\hat{\mathbf{n}} \cdot \mathbf{k} < \mathbf{0}$) with different boundary conditions to be satisfied [56, 57]. In the shadow region, the scattered fields $\mathbf{E}_s$ and $\mathbf{B}_s$ must be equal in magnitude and opposite in direction to the incident fields, respectively. However in the illuminated region, the following condition is satisfied: $\hat{\mathbf{n}} \times \mathbf{E}_s = R\hat{\mathbf{n}} \times \mathbf{E}_i$, $\hat{\mathbf{n}} \times \mathbf{B}_s = -R\hat{\mathbf{n}} \times \mathbf{B}_i$, where R is the Fresnel reflection coefficient for a TM wave.

The integral in Eq. (3.1) is now divided into two parts corresponding to the shadow (with subscript 'sh') and illuminated (with subscript 'ill') regions.

$$\begin{aligned} E_{\rm sh} &= \frac{E_0}{4\pi i}\hat{\mathbf{z}} \cdot \int_{\rm sh} (\hat{\mathbf{n}} \times (\mathbf{k}_0 \times \hat{\mathbf{z}}) + \mathbf{k} \times (\hat{\mathbf{n}} \times \hat{\mathbf{z}}))e^{i(\mathbf{k}_0 - \mathbf{k}) \cdot \mathbf{r}(\phi)} dl \\ &= \frac{E_0}{4\pi i}\hat{\mathbf{z}} \cdot \int_{\rm sh} (\mathbf{k}_0(\hat{\mathbf{n}} \cdot \hat{\mathbf{z}}) - \hat{\mathbf{z}}(\hat{\mathbf{n}} \cdot \mathbf{k}_0) + \hat{\mathbf{n}}(\mathbf{k} \cdot \hat{\mathbf{z}}) - \hat{\mathbf{z}}(\mathbf{k} \cdot \hat{\mathbf{n}}))e^{i(\mathbf{k}_0 - \mathbf{k}) \cdot \mathbf{r}(\phi)} dl \\ &= -\frac{E_0}{4\pi i} \int_{\rm sh} (\mathbf{k} + \mathbf{k}_0) \cdot \hat{\mathbf{n}} e^{i(\mathbf{k}_0 - \mathbf{k}) \cdot \mathbf{r}(\phi)} dl \ , \end{aligned} \tag{3.6}$$

$$\begin{aligned} E_{\rm ill} &= \frac{E_0}{4\pi i}\hat{\mathbf{z}} \cdot \int_{\rm ill} R(\hat{\mathbf{n}} \times (\mathbf{k}_0 \times \hat{\mathbf{z}}) - \mathbf{k} \times (\hat{\mathbf{n}} \times \hat{\mathbf{z}}))e^{i(\mathbf{k}_0 - \mathbf{k}) \cdot \mathbf{r}(\phi)} dl \\ &= \frac{E_0}{4\pi i}\hat{\mathbf{z}} \cdot \int_{\rm ill} R(\mathbf{k}_0(\hat{\mathbf{n}} \cdot \hat{\mathbf{z}}) - \hat{\mathbf{z}}(\hat{\mathbf{n}} \cdot \mathbf{k}_0) - \hat{\mathbf{n}}(\mathbf{k} \cdot \hat{\mathbf{z}}) + \hat{\mathbf{z}}(\mathbf{k} \cdot \hat{\mathbf{n}}))e^{i(\mathbf{k}_0 - \mathbf{k}) \cdot \mathbf{r}(\phi)} dl \\ &= -\frac{E_0}{4\pi i} \int_{\rm ill} R(\mathbf{k}_0 - \mathbf{k}) \cdot \hat{\mathbf{n}} e^{i(\mathbf{k}_0 - \mathbf{k}) \cdot \mathbf{r}(\phi)} dl. \end{aligned} \tag{3.7}$$

I introduce polar angles $\phi_{b1}(> 0)$ and $\phi_{b2}(< 0)$ corresponding to two

borders between the shadow and illuminated regions. For $\mathbf{k}_0$ aligned along the x-axis as shown in Fig. 3.5, we can represent the wave vector and the surface position vector as

$$\begin{aligned} \mathbf{k} &= \hat{\mathbf{x}} k \cos\theta + \hat{\mathbf{y}} k \sin\theta \,, \\ \mathbf{r}(\phi) &= \hat{\mathbf{x}} r(\phi) \cos\phi + \hat{\mathbf{y}} r(\phi) \sin\phi, \end{aligned} \tag{3.8}$$

where θ is the angle between $\mathbf{k}$ and $\mathbf{k}_0$.

Accordingly, the differential length dl and the surface normal vector $\hat{\mathbf{n}}$ are written as

$$\begin{aligned} dl &= \sqrt{[d(r\cos\phi)]^2 + [d(r\sin\phi)]^2} \,, \\ \hat{\mathbf{n}} &= [\hat{\mathbf{x}} d(r\sin\phi) - \hat{\mathbf{y}} d(r\cos\phi)]/dl. \end{aligned} \tag{3.9}$$

With these expressions, and by using an identity

$$[(1-\cos\theta)\cos\phi - \sin\theta\sin\phi]\,(1+\cos\theta) = -\sin\theta\,[\sin(\phi-\theta) + \sin\phi]\,. \tag{3.10}$$

and its counter part with $\theta \to \theta + \pi$, the preceding integrals can be rewritten as

$$
\begin{aligned}
E_{\rm sh} &= -\frac{E_0 k}{4\pi i}\int_{\phi_{b2}}^{\phi_{b1}} e^{ikr(\phi)[(1-\cos\theta)\cos\phi-\sin\theta\sin\phi]} \\
\times\quad & d\left\{r(\phi)\left[\sin\phi(1+\cos\theta)-\cos\phi\sin\theta\right]\right\} \\
&= -\frac{E_0 k}{4\pi i}\int_{\phi_{b2}}^{\phi_{b1}} e^{-ikr(\phi)\frac{\sin\theta}{1+\cos\theta}[\sin(\phi-\theta)+\sin\phi]} d\left\{r(\phi)\left[\sin(\phi-\theta)+\sin\phi\right]\right\},
\end{aligned}
\tag{3.11}
$$

$$
\begin{aligned}
E_{\rm ill} &= -\frac{E_0 k}{4\pi i}\int_{\phi_{b1}}^{\phi_{b2}+2\pi} R(\phi) e^{ikr(\phi)[(1-\cos\theta)\cos\phi-\sin\theta\sin\phi]} \\
&\times\quad d\left\{r(\phi)\left[\sin\phi(1-\cos\theta)+\cos\phi\sin\theta\right]\right\} \\
&= \frac{E_0 k}{4\pi i}\int_{\phi_{b1}}^{\phi_{b2}+2\pi} R(\phi) e^{-ikr(\phi)\frac{\sin\theta}{1+\cos\theta}[\sin(\phi-\theta)+\sin\phi]} \\
&\times\quad d\left\{r(\phi)\left[\sin(\phi-\theta)-\sin\phi\right]\right\}.
\end{aligned}
\tag{3.12}
$$

For $\theta \ll 1$ (forward diffraction) we can approximate $\sin\theta/(1+\cos\theta) \simeq \theta/2$, $\sin(\phi-\theta)+\sin\phi \simeq 2\sin(\phi-\theta/2)$ and $\sin(\phi-\theta)-\sin\phi \simeq \theta\cos\phi$, and thus $E_{\rm ill}$, proportional to θ, gives only a small contribution to the total diffracted wave in general [56, 57]. Furthermore, a significant contribution comes from the edges, where $R \simeq -1$ due to the grazing incidence of the incoming wave. Therefore, we can approximately set $R = -1$ in Eq. (3.12).

$$
E_{\rm sh} \simeq -\frac{E_0 k}{2\pi i}\int_{\phi_{b2}}^{\phi_{b1}} e^{-ik\theta r(\phi)\sin(\phi-\theta/2)} d\left\{r(\phi)\sin(\phi-\theta/2)\right\} \equiv -\frac{E_0 k}{2\pi i} X,
\tag{3.13}
$$

$$
E_{\rm ill} \simeq -\theta\frac{E_0 k}{4\pi i}\int_{\phi_{b1}}^{\phi_{b2}+2\pi} e^{-ik\theta r(\phi)\sin(\phi-\theta/2)} d\left\{r(\phi)\cos\phi\right\} \equiv -\theta\frac{E_0 k}{4\pi i} Y.
\tag{3.14}
$$

One can show that X and Y are of the same order but the former is real and the latter is purely imaginary, and thus the total intensity becomes

$$I = |E|^2 \propto |X|^2 + \theta^2 |Y|^2 \simeq |X|^2 \tag{3.15}$$

Therefore, the contribution from E_{ill} can be safely neglect.

$$E(\theta) \simeq -\frac{E_0 k}{2\pi i} \frac{e^{-ikr(\phi_{b2})\theta \sin(\phi_{b2} - \theta/2)} - e^{-ikr(\phi_{b1})\theta \sin(\phi_{b1} - \theta/2)}}{ik\theta}. \tag{3.16}$$

In addition, for two-fold symmetry with $\phi_{b2} = \phi_{b1} - \pi$ and $r(\phi_{b2}) = r(\phi_{b1})$, it is further simplified to

$$E(\theta) \simeq -\frac{E_0}{\pi i} \frac{\sin\left[kr(\phi_b)\theta \sin(\phi_b - \frac{\theta}{2})\right]}{\theta}. \tag{3.17}$$

and thus the intensity distribution becomes

$$I(\theta) \propto \frac{\sin^2\left[kr(\phi_b)\theta \sin(\phi_b - \frac{\theta}{2})\right]}{\theta^2}. \tag{3.18}$$

where I dropped the subscript '1' in ϕ_{b1} for simplicity of notation.

Now I suggest that Y in Eq. (3.14) is purely imaginary while it is in the same order as X. Since the major contribution to Y comes when $\phi' \sim \phi_{b1}, \phi_{b2}$, Y is approximately equal to

$$e^{-ik\theta y_2} \Delta x_2 + e^{-ik\theta y_1} \Delta x_1 \tag{3.19}$$

where $y_i = r(\phi_{b_i})\sin(\phi_{b_i} - \theta)$ and $\Delta x_i = \Delta[r(\phi_{b_i})\cos\phi_{b_i}]$ $(i = 1, 2)$. Assuming the two-fold symmetry with $\phi_{b2} = \phi_{b1} - \pi$ and $r(\phi_{b2}) = r(\phi_{b1})$, we have $y_1 = -y_2$ and $\Delta x_1 = -\Delta x_2 \sim -(k\theta)^{-1}$. Therefore, the second integral is proportional to

$$(e^{ik\theta y_1} - e^{-ik\theta y_1})\Delta x_1 \sim -i\frac{2\sin k\theta y_1}{k\theta} \tag{3.20}$$

showing that it is purely imaginary and its magnitude is in the same order as X.

3.3.1 Relation between the angle width function and the projected width

Let me examine what Eq. (3.17) means. First, when $\theta = 0$, the factor $w_0 \equiv r(\phi_b)\sin\phi_b$ is identified to the projected width in the exact forward direction. In the forward shadow diffraction, however, the intensity is strongly peaked at $\theta = 0$, masking the underlying diffraction pattern and thus it is necessary to measure the diffraction pattern at a slightly nonzero angle θ_0 ($\theta_0 << 1$). In this case, the quantity $w \equiv r(\phi_b)\sin(\phi_b - \theta_0/2)$ is equal to the projected width in the direction of $\theta_0/2$. This is because in the limit of $|\theta_0| << 1$ the following relation holds.

$$r(\phi_b + \theta_0/2)\sin(\phi_b) - r(\phi_b)\sin(\phi_b - \theta_0/2) \sim (\theta_0/2)^2. \tag{3.21}$$

The proof of this relation is shown below. Therefore, $w \simeq r(\phi_b + \theta/2)\sin(\phi_b)$, which is nothing but the projected width in the direction of

$\theta_0/2$.

Forward diffracted intensity $I \propto |E|^2$ then has local minima where the condition $kw\theta = m\pi$ (m is an integer) is satisfied. The angle width, the separation between two adjacent minima $\Delta\theta$ is then given by

$$\Delta\theta = \frac{\pi}{kw} \tag{3.22}$$

meaning that the angle width measured around a small forward diffraction angle θ_0 ($<< 1$) is inversely proportional to the projected width of the object in the direction of $\theta_0/2$.

Now is the time to present the proof of Eq. (3.21). Consider an object whose boundary is described by $r(\phi)$ where ϕ is the polar angle measured from the direction of the incident wave as shown in Fig. 3.2. By the definition of the border angle ϕ_b, then

$$\frac{d}{d\phi} r(\phi)\sin\phi \bigg|_{\phi_b} = r'(\phi_b)\sin\phi_b + r(\phi_b)\cos\phi_b = 0. \tag{3.23}$$

By using this, the difference $D \equiv r(\phi_b+\theta)\sin\phi_b - r(\phi_b)\sin(\phi_b-\theta)$ can be evaluated as

$$\begin{aligned}
D &\simeq [r(\phi_b) + r'(\phi_b)\theta]\sin\phi_b - r(\phi_b)\left[\sin(\phi_b)\cos\theta - \cos\phi_b\sin\theta\right] \\
&= r(\phi_b)\sin\phi_b(1-\cos\theta) + r'(\phi_b)\sin\phi_b\theta + r(\phi_b)\cos\phi_b\sin\theta \\
&\simeq r(\phi_b)\sin\phi_b(\theta^2/2) + \left[r'(\phi_b)\sin\phi_b + r(\phi_b)\cos\phi_b\right]\theta - r(\phi_b)\cos\phi_b(\theta^3/6) \\
&= r(\phi_b)\sin\phi_b(\theta^2/2) - r(\phi_b)\cos\phi_b(\theta^3/6) \\
&\sim a\theta^2,
\end{aligned} \tag{3.24}$$

where a is the mean radius. Therefore, for small $|\theta| << 1$, the difference D can be safely neglected. For example, in the experiments that will be discussed in the next section $\theta = \theta_0/2 = 2.5^\circ \simeq 0.044$, and thus the error in this approximation is only 0.1% of the mean radius of the object.

3.3.2 Examples

As an example, numerically calculated diffraction patterns are examined. Each pattern comes from a quadrupolar deformed opaque object, whose boundary is given by

$$r(\psi) = a(1 + \eta \cos 2\psi), \tag{3.25}$$

where η is a deformation parameter.

I chose the size parameter x=200 and calculated the diffraction patterns for various rotational angles ($0 \leq \beta \leq 90^\circ$) of the object. Angle widths obtained from the diffraction patterns in the direction of $\theta_0 = 5^\circ$ as a function of β are shown as dots in Fig. 3.3 for various values of the deformation parameter ($0.04 \leq \eta \leq 0.22$). The deformation parameter η is varied from 4% to 22% while the absorption Q is fixed to 100. For comparison, $w^{-1}(\beta)$, the inverse of the projection width measured in the direction of $\theta_0/2$ as a function of β is also shown for each deformation. In general excellent agreements are observed.

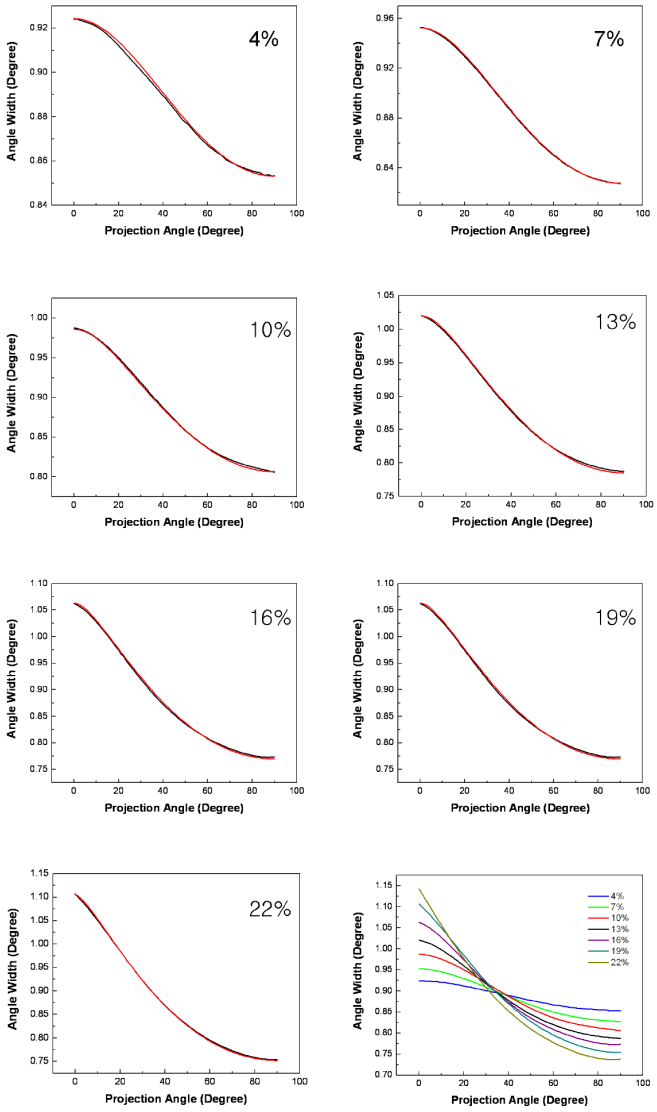

Figure 3.3: Comparison of the simulated angle width $\Delta\theta$ (black) and the inverse w^{-1} of the projected width (red) as a function of object rotation angle β for a totally absorbing quadrupole-deformed object whose boundary is given by Eq. (3.25).

3.4 Surface profiling of a two-dimensional object

3.4.1 Description of measurement geometry

Eq. (3.22) can be rewritten as

$$\Delta\theta \simeq \frac{\lambda}{2w}. \tag{3.26}$$

Then suppose that we w is repeatedly measured for various rotational angle β of the object so that $w = w(\beta)$ is obtained. The measurement geometry is shown in Fig. 3.4, where the forward direction is rotated by β with respect to the major axis of the object. Polar angle α, also measured from the major axis of the object, corresponds to the border between the shadow and illuminated regions on the object surface. If we let r the radial coordinate of the object boundary, the projected width can then be written as

$$w(\beta) = r(\alpha)\sin(\alpha - \beta). \tag{3.27}$$

3.4.2 Shape reconstruction algorithm

The task now is to find the expression for α in terms of the known quantities, such as β, $w(\beta)$ and its derivatives. Then, the radial coordinate r is given in

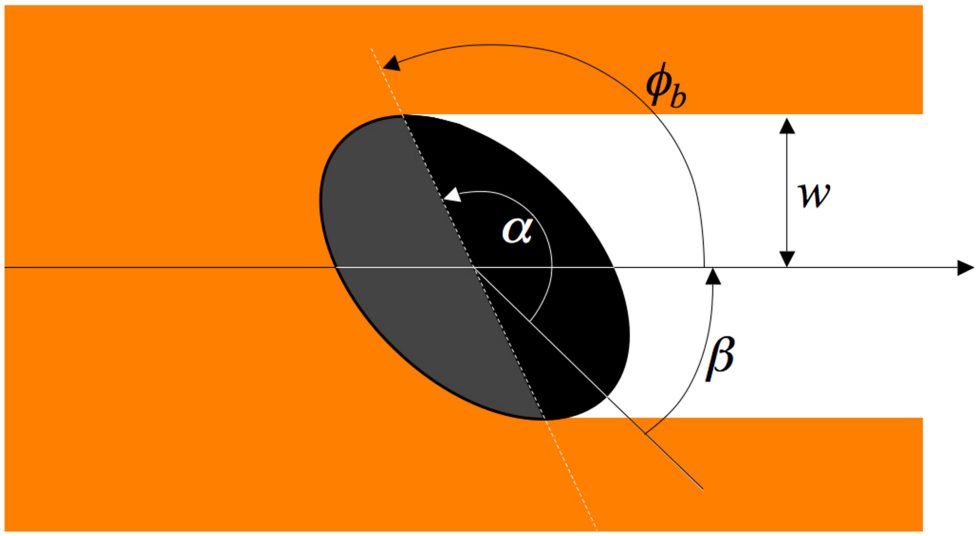

Figure 3.4: Measurement geometry for boundary profiling. Angle β is the rotation angle of the major axis respect to the forward direction. The polar angle α corresponds to the border between the shadow and illuminated regions on the object surface. The border angle ϕ_b measured from the forward direction is related to α by $\phi_b = \alpha - \beta$. Projected width w is also denoted.

terms of these quantities by Eq. (3.27) so that the geometry of the boundary is completely reconstructed.

Note that the line of tangent to the boundary at polar angle α is in the direction of β, *i.e.*, the direction of angle width ($\Delta\theta$) observation. Therefore,

$$\tan\beta = \frac{d\left[r(\alpha)\sin\alpha\right]}{d\alpha} \Big/ \frac{d\left[r(\alpha)\cos\alpha\right]}{d\alpha} \ . \tag{3.28}$$

Differentiating Eq. (3.27) with respect to β yields

$$\begin{aligned} w' \quad (\beta) &= \frac{\partial w}{\partial \beta} + \frac{\partial w}{\partial \alpha}\frac{\partial \alpha}{\partial \beta} \\ = \quad & -r(\alpha)\cos(\alpha-\beta) + \left\{ \frac{d\left[r(\alpha)\sin\alpha\right]}{d\alpha}\cos\beta - \frac{d\left[r(\alpha)\cos\alpha\right]}{d\alpha}\sin\beta \right\} \frac{d\alpha}{d\beta}. \end{aligned} \tag{3.29}$$

Due to Eq. (3.28), the quantity in the curly bracket vanishes, and therefore

$$w'(\beta) = -r(\alpha)\cos(\alpha-\beta) \ . \tag{3.30}$$

From Eq. (3.27) and Eq. (3.30), one obtain

$$\alpha = \beta - \arctan\frac{w(\beta)}{w'(\beta)} \tag{3.31}$$

and therefore

$$r\left(\beta - \arctan\frac{w(\beta)}{w'(\beta)}\right) = -\frac{w(\beta)}{\sin\left[\arctan w(\beta)/w'(\beta)\right]} \ . \tag{3.32}$$

This formula gives the radius at polar angle α in terms of the projection width $w(\beta)$ and its derivative under the constraint that the tangent at the polar angle α is in the direction of β, the direction of angle width observation. This relation holds for arbitrary β covering all angles and thus the object boundary is completely specified.

3.4.3 Projected width in the direction of angle width measurement

Comparing Fig. 3.2 and Fig. 3.4, an identification $\phi_b = \alpha - \beta$ holds. For object rotation angle β, the projection width is now written as

$$w(\beta) = r(\alpha)\sin(\alpha - \beta - \theta_0/2) \simeq r(\alpha + \theta_0/2)\sin(\alpha - \beta), \tag{3.33}$$

where an implicit functional dependence $\alpha = \alpha(\beta)$ is assumed.

Let me note that the largest angle width and thus the smallest projection width when $\beta = -\theta_0/2$ in the present convention of coordinates in Fig. 3.2 and Fig. 3.4. Explicitly, the following can be written.

$$w(-\theta_0/2) = r(\alpha + \theta_0/2)\sin(\alpha + \theta_0/2) = r(\alpha')\sin\alpha', \tag{3.34}$$

where $\alpha' \equiv \alpha + \theta_0/2$ is the polar angle at which the line of tangent at the boundary is in the direction of $\theta_0/2$. Since the object is rotated by $\beta = -\theta_0/2$, the angle α' is the same as the polar angle ϕ_b in the exact forward direction when β=0 and thus the projection width in this case is indeed the smallest.

Motivated by this observation we now make a formal substitution $\beta' = \beta + \theta_0/2$ and $\alpha' = \alpha + \theta_0/2$ so that

$$w(\beta') = r(\alpha')\sin(\alpha' - \beta'). \tag{3.35}$$

Under this coordinate transformation, the resulting projected width is equivalent to the projected width in the exact forward direction in the shifted coordinate $\beta' = \beta + \theta_0/2$. Since only the function dependence of $w(\beta')$ matters for the surface profiling technique, all primes in Eq. (3.35) can be dropped and then the same form as Eq. (3.27) is obtained:

$$w(\beta) = r(\alpha)\sin(\alpha - \beta). \tag{3.36}$$

3.4.4 What happens if the two-fold symmetry is not there?

In order to answer this question, we go back to Eq. (3.16)

$$E(\theta) \simeq \frac{E_0}{2\pi\theta}\left[e^{-ikr(\phi_{b2})\theta\sin(\phi_{b2}-\theta/2)} - e^{-ikr(\phi_{b1})\theta\sin(\phi_{b1}-\theta/2)}\right], \tag{3.37}$$

which gives an intensity distribution of

$$I(\theta) \propto \frac{\sin^2\left[k\theta(w_1 + w_2)/2\right]}{\theta^2}, \tag{3.38}$$

where $w_1 = r(\phi_{b1})\sin(\phi_{b1} - \theta/2)$ and $w_2 = r(\phi_{b2})\sin(|\phi_{b2}| + \theta/2)$ (note $\phi_{b1} > 0, \phi_{b2} < 0$). By similar approximation to Eq. 3.21, it can be shown that $w_1 \simeq r(\phi_{b1} + \theta/2)\sin(\phi_{b1})$ and $w_2 \simeq r(\phi_{b2} + \theta/2)\sin(|\phi_{b2}|)$, which are nothing but the upper and lower projected widths or radii in the direction of $\theta/2$, respectively. The angle width to be observed is then proportional to the inverse of the mean projected width $\bar{w} \equiv (w_1 + w_2)/2$.

If there is no two-fold symmetry, the projected widths w_1 and w_2 are not equal in general. Since only the mean projected width $\bar{w}$ is measured as a function of the object rotational angle β in the present scheme, w_1 and w_2 are not separately known and thus there is no sufficient information to reconstruct the boundary shape. Of course, if w_1 and w_2 are separately known by some means, one can reconstruct the boundary shape by the similar reconstruction algorithm.

There are several ideas to separate w_1 and w_2. One is to employ a reference plane wave with a known tilt angle with respect to the incident plane wave in order to encode a phase shift information in the diffraction pattern in the case of displaced object center. Another idea, applicable to a transparent object, is to utilize refraction for decoding the information on the object center. This idea is rooted in the fact that the angle width in a near forward direction ($\theta << 1$) is still inversely proportional to the projected width even when the object is semi-transparent. This fact can be observed in Fig. 3.1, where the distance between the first and third off-axis intensity minima is almost independent of the absorption coefficient of the object. Since refraction depends on the object shape, one might be able to decode the information on the object center from the total diffrac-

tion/refraction pattern. In addition, the above observation also suggests that the requirement on opaqueness is not very stringent for the present technique. Quantitative investigation on these subjects is left for a future study.

3.4.5 Examples of the shape reconstruction and an accuracy evaluation

In order to test both usefulness and accuracy of this shape reconstruction technique, I apply the technique to a quadrupolar-deformed opaque object whose boundary is given by Eq. (3.25).

The polar angle ψ is now set to be measured from the major axis of the object. The first case to be considered is $\eta = 0.16$ with a size parameter of 190. From the angle width function $w(\beta)$ obtained from the calculated diffraction patterns for various β, reconstructed $r(\phi)$ show a good agreement with Eq. (3.25) for $\eta = 0.159 \pm 0.002$.

Another test was done on a quadru-octapolar object whose shape is given by the expression:

$$r(\psi) = a(1 + \eta_1 \cos 2\psi + \eta_2 \cos 4\psi) \ . \tag{3.39}$$

For the ratio (quadrupole : octapole) = (94 : 6) with $\eta_1 = 0.160$ and $\eta_2 = 0.0102$ and with a size parameter of 190.0, the result of reconstruction was $\eta_1 = 0.160 \pm 0.001$ and $\eta_2 = 0.009 \pm 0.001$). The reconstructed boundary

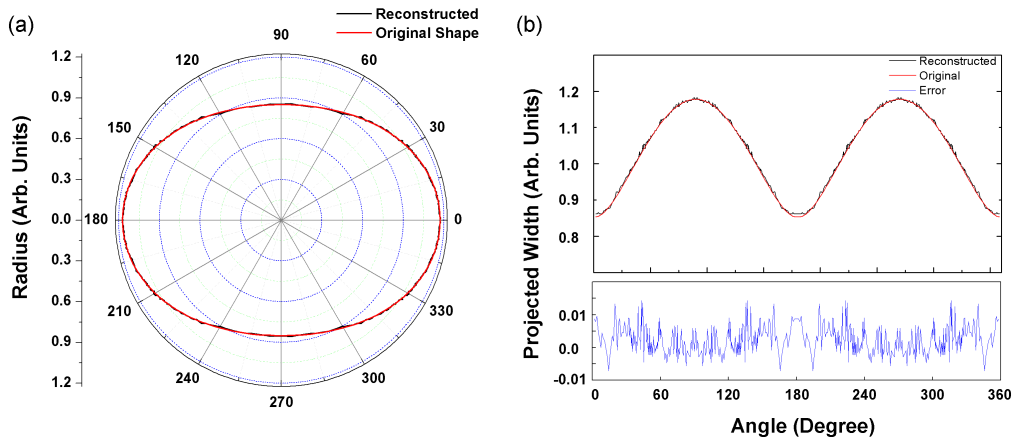

Figure 3.5: (a) Reconstructed boundary profile (in black, non- smoothed) obtained from calculated diffraction patterns for an opaque cylindrical object whose boundary (in red, smooth curve) is described by Eq. (3.39) with $\eta_1 = 0.16$ and $\eta_2 = 0.01$. (b) Projected width w as a function of β. The difference between the reconstructed width (in black) and the actual width (in red) is also shown (in blue).

shape is shown in Fig. 3.5(a). Projected width w as a function of the object rotation angle β for the same case is displayed in Fig. 3.5(b). The difference between the reconstructed width and the actual width is also shown below. One can smooth the original data to avoid erratic discrepancy seen in Fig. 3.5(b), however, it makes no meaningful change for a reconstruction result.

Another testing example is a quadru-octapole shape with the ratio (quadrupole : octapole) = (91 : 9), $\eta_1 = 0.2002$ and $\eta_2 = 0.0198$. From the calculated diffraction patterns for a size parameter of 190.0, we recovered $\eta_1 = 0.201 \pm 0.001$ and $\eta_2 = 0.02 \pm 0.001$.

I also apply the reconstruction technique to various pure quadrupoles with η varied from 0.02 to 0.19 and try to fit the reconstructed shape with the quadru-octapole formula of Eq. (3.37) intentionally. The purpose of this test is to check the robustness and the sensitivity of the reconstruction algorithm. The results are summarized in table 3.1. The erroneous octapole component is typically 0.002, which can be considered as as a typical sensitivity in probing high order deformation components in our technique.

real quadrupole deformation	reconstructed quadrupole η_1	reconstructed octapole η_2
0.02	1.9($\pm$0.001)	-0.001($\pm$0.001)
0.04	3.9($\pm$0.001)	-0.001($\pm$0.001)
0.07	6.9($\pm$0.001)	-0.001($\pm$0.001)
0.10	10.0($\pm$0.003)	0.002($\pm$0.002)
0.13	12.8($\pm$0.002)	-0.003($\pm$0.002)
0.16	15.9($\pm$0.002)	-0.002($\pm$0.001)
0.19	19.0($\pm$0.001)	-0.001($\pm$0.002)

Table 3.1: Reconstructed shape parameters of various pure quadrupolar objects ($0.02 \leq \eta \leq 0.19$) with a common size parameter of 200. Reconstructed boundary profiles are intentionally fitted to the quadru-octapole shape of Eq. (3.39) in order to test the robustness and sensitivity of the present reconstruction technique. The resulting fit parameters are listed.

Chapter 4

Surface reconstruction of the liquid microjet and identification of internal modes

4.1 Realization of the surface mapping method

To realize the surface mapping method introduced in the previous chapter and apply it to a liquid microjet, the liquid should be effectively opaqueness. This is accomplished by heavy doping of the dye material. Required condition to be needed is satisfied when the optical density due to absorption for a laser beam going through the diameter exceeds 6.9. Fig. 4.1 shows the extinction coefficient of Rhodamine 590 dye within region of visible wavelength. In experiment which I will discuss here a TM-polarized cw-laser at 532 nm (or 514 nm in some cases) is used as observing beam. According to

the extinction coefficient data [58], absorption cross section σ at λ=532 nm is 3×10^{-21} m^2. It corresponds to a molar density of 23.3 mM/L when the dye is dissolved in ethanol at $20°C$. For safe guarantee, I take 30.0 mM/L, approximately 30% higher than the bare standard, as the density of the dye material.

The experimental setup is depicted in Fig. 4.2. The liquid jet system is mounted on a rotary stage, to take diffraction patterns for an arbitrary rotation angle. And the vertically ejected jet is illuminated by observing laser beam, which is tightly focused by a cylindrical lens down to a vertical waist of 3 μm on the jet. The diffraction pattern of the laser beam by the jet column is then examined on a screen located at 2.4 m from the jet. The mean radius of the jet column is about 15 μm while the horizontal waist of the laser beam is 2.3 mm, fully covering the jet column horizontally.

Like the test with the simulated diffractions, about $5 \sim 6$ local minima lying within 10.0 degrees from the forward direction are used to obtain a mean value of $\Delta\theta$ for a given rotation angle β of the jet assembly. The typical value of the resulting $\Delta\theta$ is about 1 degree. Collecting $\Delta\theta$ as a function of θ leads the reconstruction procedure as it is described in the previous chapter. Fig. 4.3(a) shows an example of the "anglewidth function" and Fig. 4.3(b) the reconstructed result from the former. The example is obtained at the following experimental conditions : an ejection pressure of 2.6 bar, $a = 15 \pm 1\mu$m, $v_z = 16.0 \pm 0.1$ m/s, and the position is D3 (height of 860 μm from the orifice). The magnitudes of the quadrupole and octapole components there are 23.9($\pm$0.3)% and 2.6($\pm$0.2)% of the mean radius, respectively. The magnitudes of the higher poles are smaller than

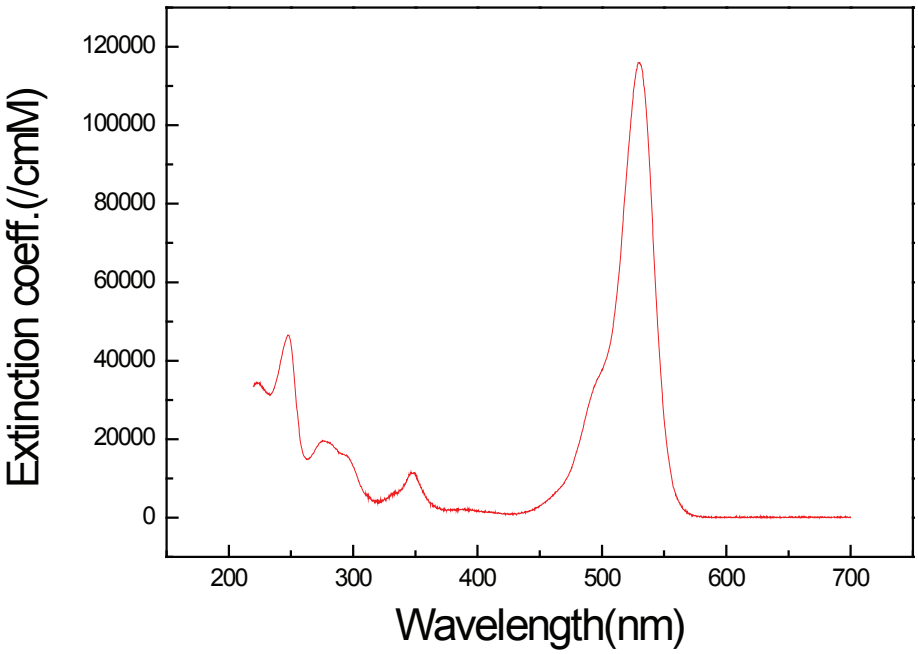

Figure 4.1: The extinction coefficient of Rhodamine 590 from 200nm to 700nm [58].

0.1%, which is within the error range of the present technique.

4.2 Relation between the quadrupolar and octapolar components

4.2.1 General remarks on the reconstructed profiles

The measurement of $\Delta\Theta$ is repeated for various initial conditions such as different ejection pressure, types of solvent and mean radii at several extreme positions on the jet.

All boundary profiles we reconstructed exhibit 2-fold axial symmetry. The profiles are dominated by a quadrupolar component. The second largest component is a octapole component. The magnitude of the octapole component in almost all cases cannot be explained by the linear theory. Its failure is once more evident. For example, let us examine the profile derived in Fig. 4.3(b). i.e. $23.9(\pm 0.3)\%$ quadrupole and $2.6(\pm 0.2)\%$ octapole. I remind that the data is obtained at the height of 860 μm from the orifice. Therefore, if the linear theory were correct, the observed magnitude of the octapole component should come from an initial relative magnitude exceeding $15,000\%$, which is simply impossible.

4.2.2 Measuring B

Now, finally we are at the critical point. From data for various conditions, Eq. (2.38), the theoretical relation between quadrupolar and octapolar components, can be attested. Figure Fig. 4.4 summarizes the B values extracted

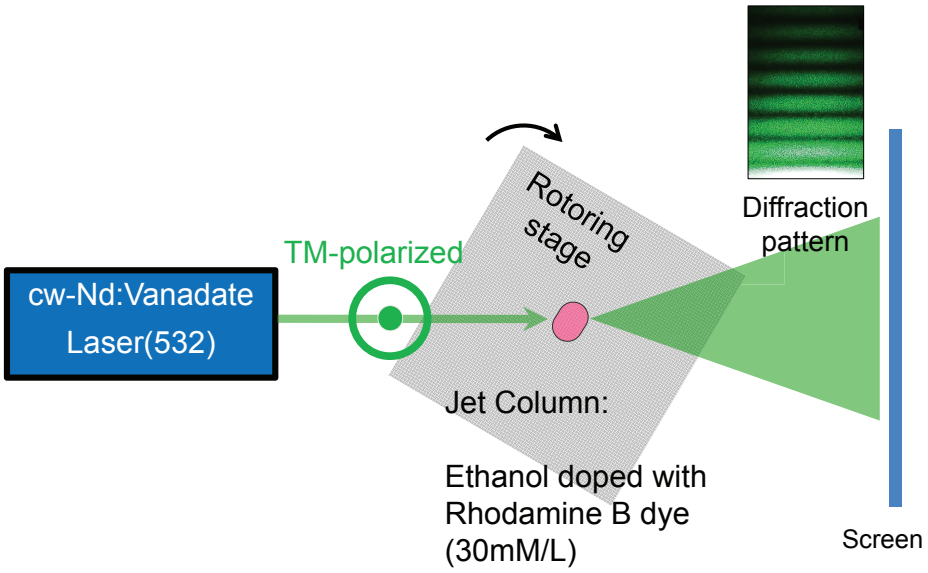

Figure 4.2: Experimental setup of the surface mapping of a microjet. An example of real image of the diffraction pattern is provided on the inset.

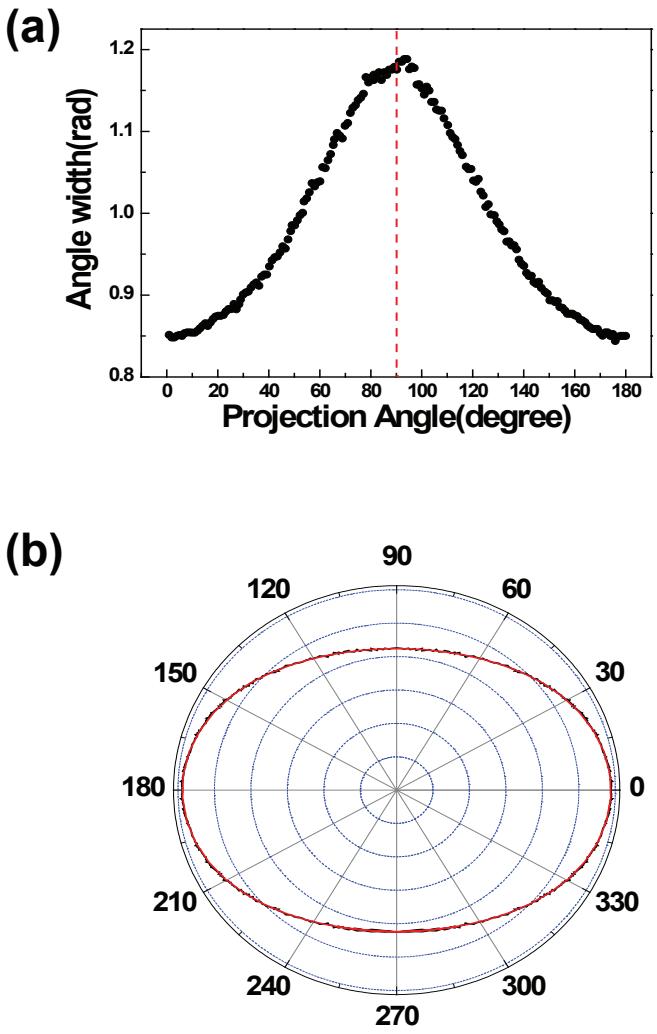

Figure 4.3: (a)An example of the anglewidth function. Dashed line in the middle of the graph indicates the axis of symmetry. (b)Reconstructed profile from data (a).

from the observed boundary profiles under different conditions such as the size parameter x, types of solvent and the magnitude of quadrupolar deformation. Black squares and red circles are data of ethanol, while green down-triangles blue up-triangles are that of ethanol+water 50:50 mixed solution. Numbers remarked in the legend is x.

The result is remarkable. It shows clear tendency that data are centered around a constant value, $B = 0.42 \pm 0.08$, despite the different experimental conditions. Note that the measured values of B are clearly separated with that of an ellipse(red line at 0.75).

4.2.3 Discussion on the result

Before drawing any conclusion, however, there are a few issues I must argue about the result. A part of data in Fig. 4.4, especially the black squares, may give an impression that B has the growing tendency with the quadrupolar deformation. I think this is not true for two reasons. First, the most probable part where B grows as if it has such tendency is where the deformation is very small. For example, when the quadrupolar deformation is recorded as 0.085, the octapolar deformation is only 0.0015, that corresponds $20nm$ of radial deviation at most. That is the limit of the resolution of the surface mapping method. i.e. about 0.1% of the radius. Due to the difficulty for detecting small magnitude of the component, data there have relatively large error bars. Second, other data within the region does not exhibit such tendency. Therefore I interpret the 'growing tendency' is just a phantom emerged from the experimental error.

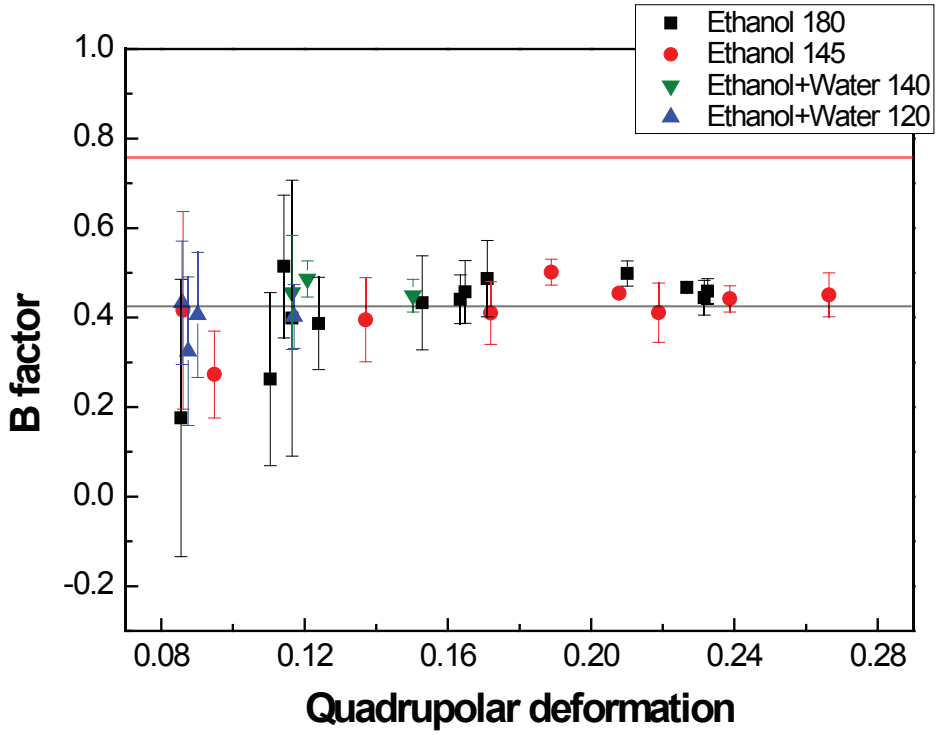

Figure 4.4: Measured B factors for various quadrupolar deformations, x, and materials. Ethanol/Ethanol+Water in legend denotes the material, while the numbers indicate x. Average line is drawn at $B = 0.42$ horizontally.

Thus, empirically, the boundary profile can then be described by the following equation:

$$r/a \simeq 1 + \eta \cos 2\theta + 0.42\eta^2 \cos 4\theta, \tag{4.1}$$

Note that η on the above relation is different from the same notation had indicated in chapter 2 in rigorous sense. Because Eq. (4.1) do not contain the area conservation term. If we rewrite Eq. (2.18) with changing $\eta \rightarrow H$ and $5/12 \rightarrow B_c$, then

$$r/a = 1 - \frac{1}{4}H^2 + H \cos 2\theta + B_c H^2 \cos 4\theta. \tag{4.2}$$

According to this, experimentally measured B is actually $B_c(1 - H^2/4)$. Again it is very tempting to suppose that measured B has a growing tendency with η. But I have already refused it. A correction of $H^2/4 \sim \eta^2/4$ changes B $1 \sim 2\%$ at most. Such a small variation can not be confirmed by the surface mapping technique. Let me consider one more issue. If we respect the theoretically derived value, 0.42 would be changed to $B_c \sim 0.41$. In fact, it is in the range of error. But I am not convinced which one gives more "accurate" description. Even at the regime that quadrupolar deformation is $0.2 \sim 0.3$, two cases deviate only less than 10 nm along the radial coordinate. That is also out of resolving power. Still, the error range can be reduced by extensive comparison between results of the spectroscopic experiment and the numerical calculations, which will be discussed in the last section of this chapter. But I see even after doing that, no clear indication that which is more reliable.

4.3 Analyzing tools of the spectroscopic experiments

4.3.1 Free spectral range and the locally repeated structure in a CMF spectrum

In section 2.4 I represented a huge discrepancy of the positions of cavity resonances between experimental observation and numerical simulation, performed with the incomplete theoretical boundary profile, Eq. (2.15). The incompleteness has been hitherto revised. Before back to this problem, special tools for analyzing will be discussed.

The quasi-modes found experimentally in this study generally show rather high quality factors: a few $1,000 \sim 10^6$. This observation indicates that the high-intensity region of the wave intensity distribution of the observed resonances are localized near the boundary of the cavity, much like the well-known whispering gallery modes. Thus in the theoretical point of view the free spectral range(FSR)s have similar value (with modification) to that of the periodic circular orbit of the same radius. The latter is given by

$$\Delta\lambda = \frac{\lambda^2}{2\pi n a}, \tag{4.3}$$

where a is the radius, λ is the wavelength of the reference resonance, and n is the index of refraction. In this respect, the repeat of the similar structure of the quasi-modes with the cycle of about 3nm in Fig. 2.4 is unsurprising,

because the experimental conditions are roughly $a{\sim}14\mu m$, $\lambda{\sim}585nm$, and $n{\sim}1.36$ and they lead $\Delta\lambda{\sim}2.86nm$. These argument for the FSR are helpful for constructing the following tools.

4.3.2 Grouping of the quasi-modes in the cavity-modified fluorescence spectrum

It is noteworthy that the visible resonances in the CMF spectrum obtained from the microjet cavity system have well-defined free spectral range (FSR)s within my experimental observations. And it is always possible to construct sequences of quasi-modes of which FSR functions are piece-wisely slowly-varying (if there are discontinuous point, the successive position of the sequence is determined for the striding gap to be minimized) and assign any quasi-mode on one of them. These sequences are already noted as the "groups" of quasi modes.

To describe the grouping more visually, let me revisit the spectrum data in Fig. 2.5. Fig. 4.5 shows the spectrum again (on the upper part of the figure), markings of the all positions of the quasi-modes (arranged horizontally along the intensity=$2,000$ line for the spectrum data) , and re-representation of those markings by separating them into 5 groups as the principle above mentioned (on the bottom). Each group is denoted to a number by bottom-to-top order, namely group 1 to group 5. This ordering is not arbitrary, though conventional in a way, and will be explained later.

For most of the cases the FSR functions of each sequences varies slowly between about 2.8∼3nm. Other choices make overall vibration of the FSR

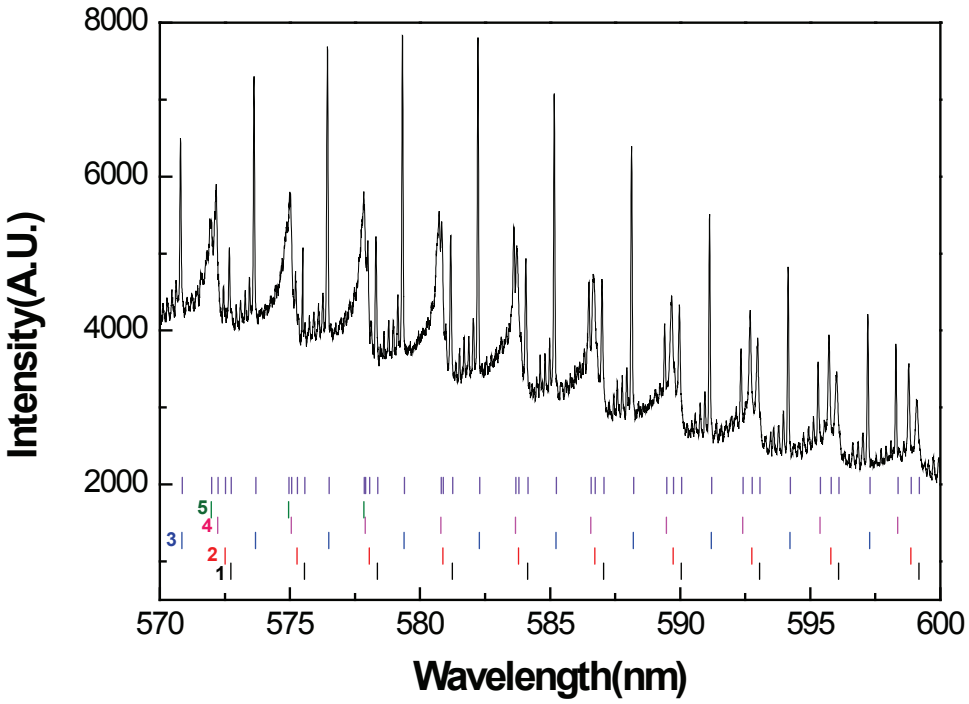

Figure 4.5: An example of the extraction of quasi-modes from the spectrum data and their grouping.

functions much stronger. For example, if 574.997nm is chosen as the next of 570.794nm, instead of 573.617nm, FSR between two is 4.203nm. Then whatever choice comes next, similar FSR within $\pm 0.1nm$ (which is easily accomplished from the grouping presented in Fig. 4.5) cannot be obtained because the candidates in order are $575.212nm$, $575.499nm$, $576.439nm$, $577.784nm$, $577.837nm$, $577.995nm$, $578.306nm$, $579.322nm$, and so on. An example of the discontinuity above mentioned is found at 580.823nm and 580.737nm. Two quasi-modes are very close to each other. Therefore it might be ambiguous to determine what sequence each of them belongs to and what is the next to it. In this case, 580.823nm is assigned on the group 2 while 580.737nm on the group 4, because this choice allows the least local change of the tendency of each FSR function. Specifically, if 580.737nm is chosen as the next of 577.995nm, the growing tendency of FSR function of the group 2 suddenly reversed.

4.3.3 Quasi-mode evolution diagram

By the way, the style of Fig. 4.5 as a representation of the positions of quasi-modes is rather complicated for grasping their evolution at a glance. This is the reason why the quasi-mode evolution diagram is developed. Basic description of the diagram is introduced in the section(to be updated). Here are more detailed informations.

To construct the diagram, the positions of the quasi-modes are transformed into X, the relative size parameter that is defined as following relation.

$$X = \frac{2\pi na}{1.361\lambda}, \tag{4.4}$$

where n is the index of refraction, a is the radius, and λ is the wavelength of the targeted quasi-mode. 1.361 is the index of refraction of ethanol at 20°C, and $\lambda = 610$nm. In reality, n/λ must be carefully calibrated to be used for precise co-matching between the experiments and the numerical calculations, because of three major factors: the intrinsic calibration error of the detector (spectrometer), the temperature dispersion of the index of refraction, and the wavelength dispersion of the index of refraction. However, this calibration do not changes the macroscopic-relative behaviour of the quasi-mode groups (See Appendix B).

The quasi-mode evolution diagram shows the transformed positions of quasi-modes relative to each reference. The references are taken from a virtual sequence of X of which spacings are regular. Conventionally the intersection and the magnitude of the spacing of the reference sequence are set to make the most par of the resulting group 3 be approximately put on the horizontal 0 line. This convention is inspired from that it is easy to treat the group 3 as the temporal reference in the coarse of the experiments, because as shown in Fig. 4.4 over a wide range the members of the group 3 are apart from other group members thus show "noble" behaviour, and therefore one can easily recognize them.

Fig. 4.6 is an another example of the experimental quasi-mode evolution diagram. It is obtained from the spectrum data got under the conditions 1.188bar (ejection pressure), D4 (vertical position), 20.3°C (room temper-

ature), and 14 ± 1 μm (mean radius). Jet material is ethanol doped with 0.05mM/L of Rhodamine 6G dye. It shows the typical features of the behaviours of the quasi-mode groups observed for the most of the surveyed conditions. There are 5 distinguishable quasi-mode groups, and 3 avoided crossing and 1 crossing between them. $3-4$, $1-2$, and $2-4$. And 5 penetrates 4 (namely, crossing occurs). group 3 and 4 avoid each other. The avoided-crossing behaviours of the groups are related to that the groups interact to each other. The gap between two groups at the nearest approach (denoted to the "avoided crossing gap") offers a measure for the relative strength of the interaction : the wider the gap, the stronger the interaction. When the avoided crossing occurs, the inclinations of the diabatic lines that two groups follow are considerably varied, as if they are exchanged.

The group 1 and 2 approach to each other beyond $X \sim 145$ and it is expectable that they will cross or once again avoid soon. In fact, there are strong evidences that suggest $1-2$ avoid around $X \sim 150$. In the represented results, the group 1 and 2 are invisible beyond $X \sim 149$ because the output couplings are too low there due to their high quality factors. However, it can be noted that at the other doping condition the avoided crossing between the group 1 and 2 clearly appears [24]. Additionally, it is expected that the avoided crossing of $2-4$ is altered to the crossing below a certain threshold of the eccentricity. Verification of it is one of the future task. Please see Appendix C.

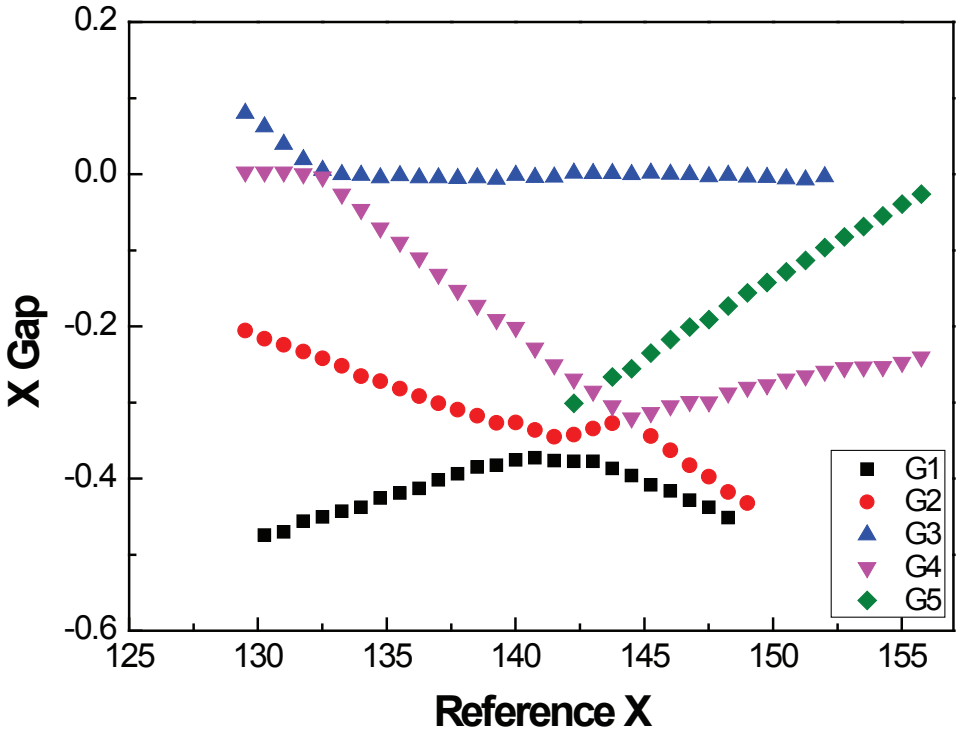

Figure 4.6: Quasi-mode evolution diagram for 1.188bar, D4, 20.3°C, and 14 ± 1 μm.

4.3.4 The ordering of the quasi-mode groups

Now is the time to state about the ordering. Basically the ordering of the quasi-mode groups is the order of the magnitudes of their FSRs in a wavelength region exists below the nearest approach of the group 1 and 2 (Actually, over 5∼6 FSRs). Namely in this region FSR of group 5 is the largest, and that of group 1 is the smallest. This ordering is first introduced in the reference [5] and thenceforth used by the authors including me. The special notice of that region is related to that the quasi-mode groups there do not cross or avoid and follow each diabatic line well, thus behave as if they are uncoupled. The *letter* "as if" is indispensable, because the groups still do interact there, but the influences are not so evident.

A practical problem for the application in this study is, like Fig. 4.6 the group 1 and 2 are invisible there in many cases. Therefore in fact it is based on the assumption that the group 1 and 2 avoid once again that the identification of group 1 to be really 1 according to the above definition.

4.4 Identification of the internal high-Q modes

4.4.1 Preparations

Now, the comparison between the experimental result and the numerical simulation will be presented. To carry out it, CMF spectrum for various experimental conditions are measured. Dye material is Rhodamine 590 with density 0.05 mM/L. Room temperature is around 20.0°C. Under such conditions, the best visible range of wavelength for the cavity modes which

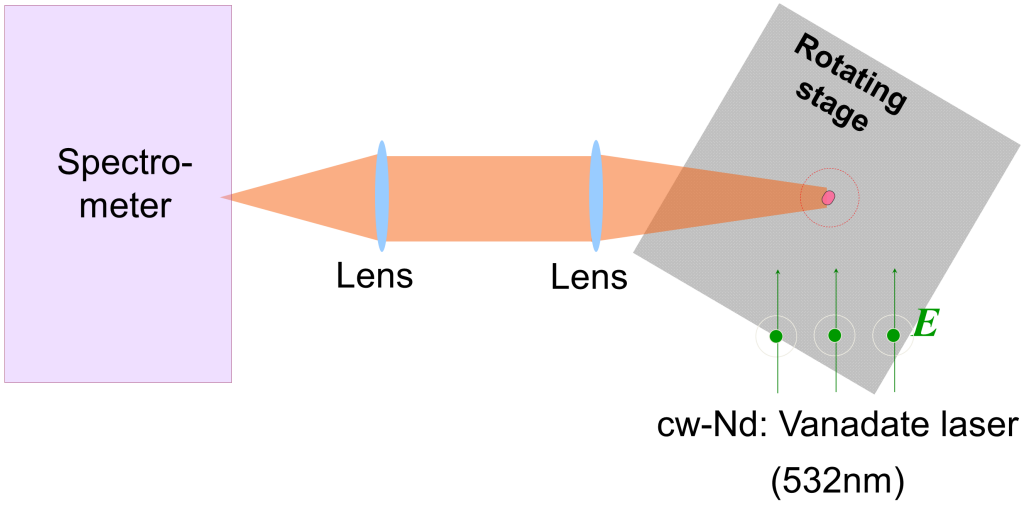

Figure 4.7: Experimental setup for CMF spectroscopy. Incident laser beam is TM-polarized.

appear as the resonance in the CMF spectrum is between about 550 nm and about 650 nm. The experimental setup is displayed in Fig. 4.7. The spectrometer used here is a double-monochromator whose resolution is 0.05 nm.

The pressure 1∼2bar, CMF spectrum is usually clearly visible between D2∼5. Various factors limit the visibility. D1 is in many cases not recommendable, because the deformation there can be too large. Even an evidences for the break of the convexity is often observed : the shadowed region appear on the middle of the cavity on the CCD image. This implies that the boundary has a peanut-like shape. If the boundary is quadrupolar-deformed one, over $\epsilon = 0.20$ this kind of the broken convexity occurs.(See Fig. 4.8) On the contrary at the positions beyond them, the surface oscillation of the cavity is pacified to far and the internal modes with extreme high-Q are hard to be out-coupled sufficiently.

For the numerical calculation, Eq. (4.1) is used as the boundary profile except only one change : B is 0.41 rather than 0.42, because this is theoretical, not empirical.

The following features are sensitive to the boundary shape in the calculations and have worth to receive attention : the interval between $3-4$ avoided crossing and $2-4$ avoided crossing, the relative position where 5 crosses 4, the avoided crossing gap of $2-4$, the avoided crossing gap of $1-2$, and so on.

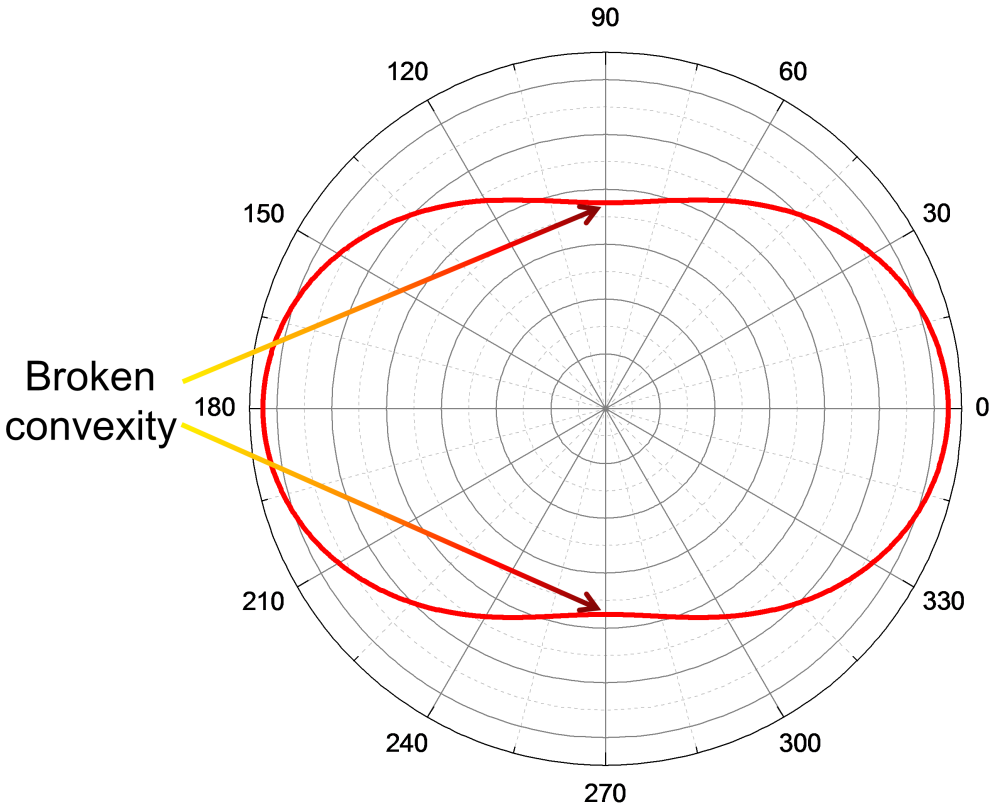

Figure 4.8: Quadrupolar-deformed($\eta = 0.25$) cavity boundary.

4.4.2 Matching of the quasi-mode evolution diagram

A matching is tried around the expected eccentricity with changing η by 0.05. The best fit results show remarkably good agreements. For example, Fig. 4.9 is the matched result for the repeatedly mentioned 1.408bar-D4 experiment. At $\eta = 0.185$ the best fit within the examination is accomplished. The group 4 after $3-4$ avoided crossing covers 19 FSRs until $2-4$ avoided crossing. 5 penetrates 4 during the same quasi-mode packet where $2-4$ avoid. Careful calibration leads that the absolute positions of each quasi-mode can be astonishingly fit to the counterpart from the calculation.

It is possible to find such a best matching for any experimentally observed spectrum data. Another examples are displayed on Fig. 4.10, Fig. 4.11, and Fig. 4.12. 1.326bar-D5-20.3°C-14 $\pm$ 1 μm data are matched with the calculation for $\eta = 0.125$ (Fig. 4.10). For 1.188bar-D4-20.3°C-14 $\pm$ 1 μm, $\eta = 0.16$ (Fig. 4.11). And for 1.536bar-D4-19.1°C-14 $\pm$ 1 μm, $\eta = 0.20$ (Fig. 4.12). Half of the trying interval can be allowed as the matching error, namely ± 0.0025.

The matching is equivalent to the one-to-one identification of each experimentally observed quasi-mode in a form of $nka = n2\pi a/\lambda$ to a theoretically recovered resonance. It is helpful to make a experimental data sheet of noticeable key features sensitive to η. In table 4.1 I collect 3 of them. The number of FSRs group 4 covers between $3-4$ and $2-4$ avoided crossing (denoted to $3-4$ to $2-4$), The relative position(FSRs) where 5 penetrates 4 to $2-4$ avoided crossing (denoted to $4-5$ to $2-4$), the avoided crossing gap of $2-4$ (denoted to ACG). ACG is the local minimum value of a quadratic

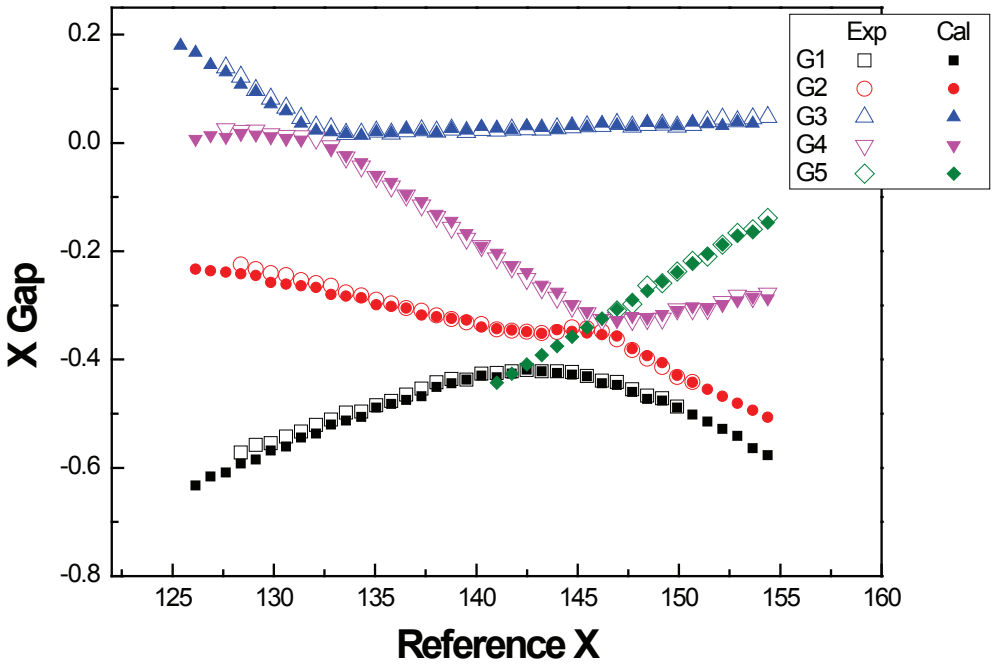

Figure 4.9: A matched quasi-mode evolution diagram for the experimental data obtained at 1.408bar-D4-19.5°C-14 $\pm$ 1 μm.

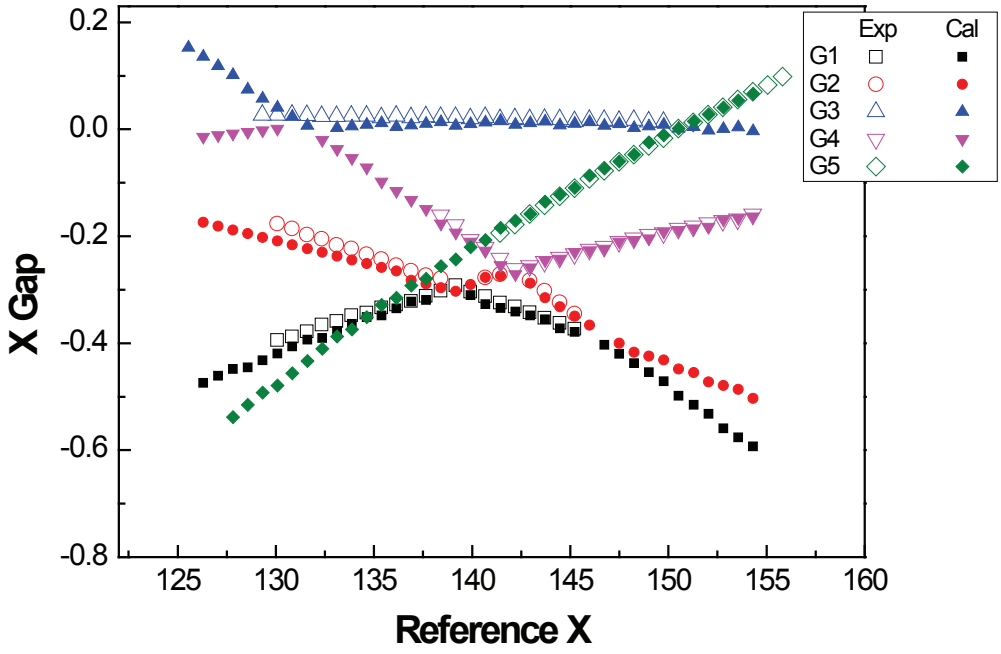

Figure 4.10: Qausi-mode diagram matching. 'Exp' denotes experimental data at 1.326bar-D5-20.3°C-14 $\pm$ 1 μm and 'Cal' denotes numerically simulated data for $\eta = 0.125$.

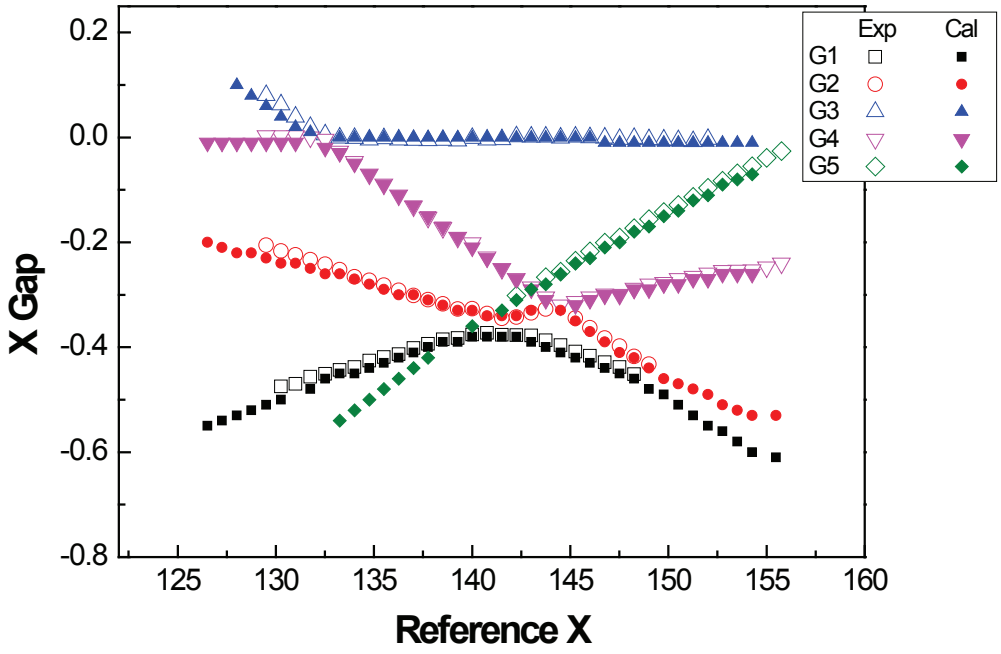

Figure 4.11: Qausi-mode diagram matching. 'Exp' denotes experimental data at 1.188bar-D4-20.3°C-14 $\pm$ 1 μm and 'Cal' denotes numerically simulated data for $\eta = 0.16$.

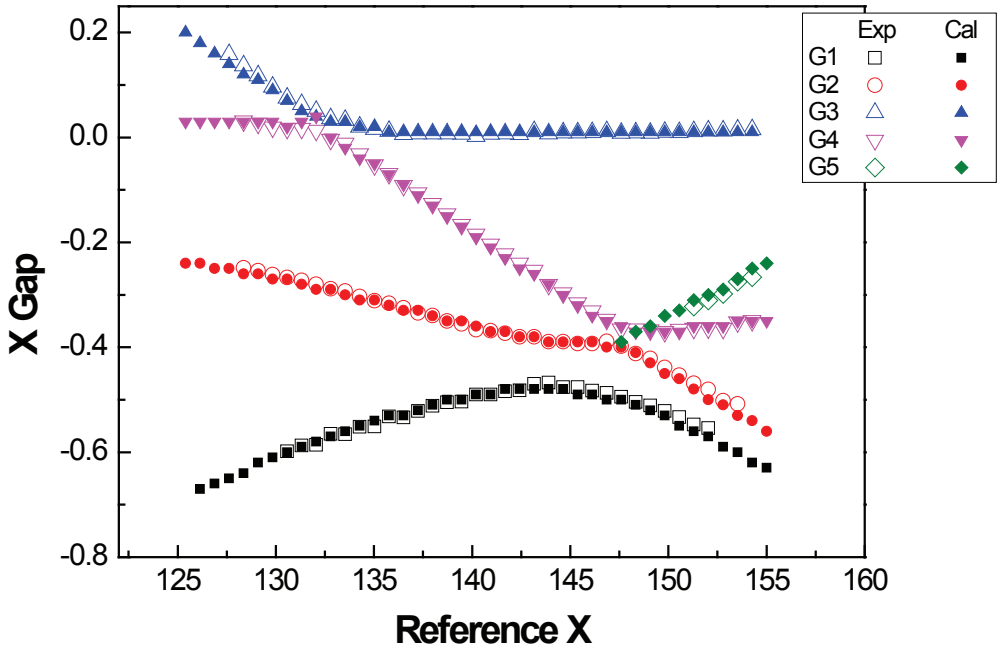

Figure 4.12: Qausi-mode diagram matching. 'Exp' denotes experimental data at 1.536bar-D4-19.1°C-14 $\pm$ 1 μm and 'Cal' denotes numerically simulated data for $\eta = 0.20$.

fitting curve around the position where the avoided crossing occurs. There are other data which are not presented here because of their insufficient information. However, these data do not disturb the tendencies emerge on the table 4.1. At $\eta = 0.125 \pm 0.0025$, $2 - 4$ avoided crossing is too sharp to be analyzed by a quadratic fitting. For now, I am afraid to say more than that ACG is smaller than 0.01 there.

η	$3-4$ to $2-4$	$4-5$ to $2-4$	ACG
0.125($\pm$0.0025)	14	-3	very small
0.16($\pm$0.0025)	17	-1	0.016($\pm$0.011)
0.185($\pm$0.0025)	19	0	0.025($\pm$0.004)
0.20($\pm$0.0025)	21	+1	0.039($\pm$0.006)

Table 4.1: Reference data set of dynamical feature of quasi-mode groups. +(-) sign in the $4-$ to $2-4$ column denotes that the $4-5$ crossing occurs at higher(lower) X than $2-4$ avoided crossing. Error range of ACG is due to the fitting error.

4.4.3 A consideration of the avoided crossing gap and the tolerance of the reconstructed profile

Weak interaction between the group 2 and 4 make their avoided crossing gap one of subtle features of the quasi-mode evolution. At Fig. 4.10 the two sequences almost overlapped each other. At Fig. 4.12 however, one can notice that the two sequences are sufficiently apart to be resolvable even in the large-scale diagram.

The avoided crossing gaps are also useful for verifying the boundary shape. That is to say, they can be another evidences of Eq. (4.1). In Fig. 4.13, $2-4$ avoided crossing gaps are compared to the calculated value for various B factors from 0.37 to 0.45 The horizontal axis is the eccentricity. The gap become larger with η, and smaller with B. *i.e.* At the same η smaller B makes the interaction between $2-4$ stronger. Experimentally measured gaps are appeared between the calculated values for $B = 0.39$ and $B = 0.43$, accompanied the error bars. The result indicates that the experimental B factor falls on 0.415 ± 0.010. This is the most accurate value which I can offer as the experimental B factor up to this time. More fine resolving is rather limited. Fig. 4.14 shows both simulated quasi-mode evolution diagram with $\eta = 0.19$ but B is 0.41 and 0.42 respectively. Two diagrams exhibit only slight deviation. If this amount of deviation is observed from the real CMF spectrum, it would be probably regarded as a result of experimental error such as a little failure of calibrating or vibrations of conditions.

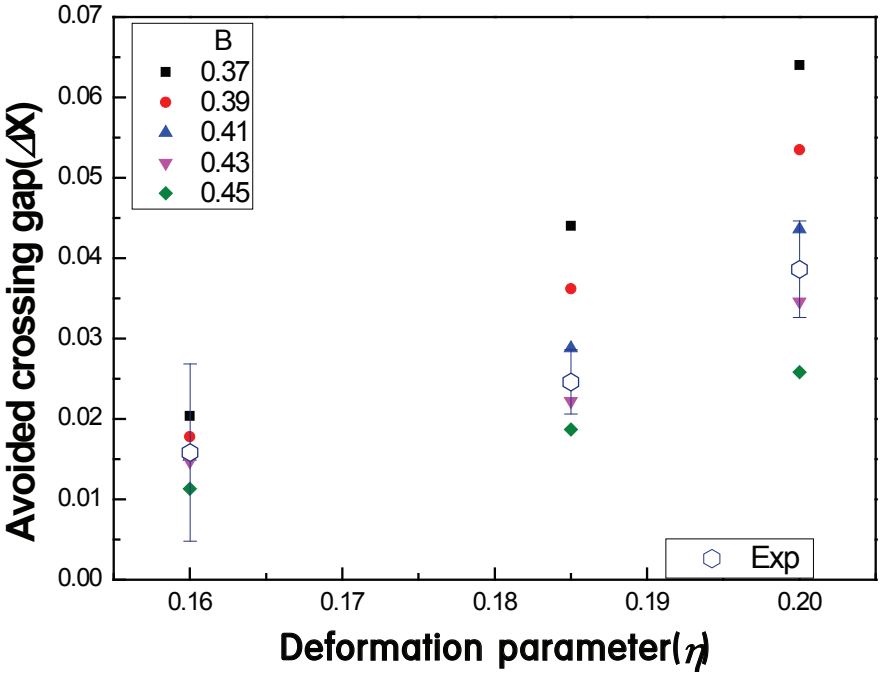

Figure 4.13: $2-4$ avoided crossing gaps for various η and calculated values with varying B factor from 0.37 to 0.45.

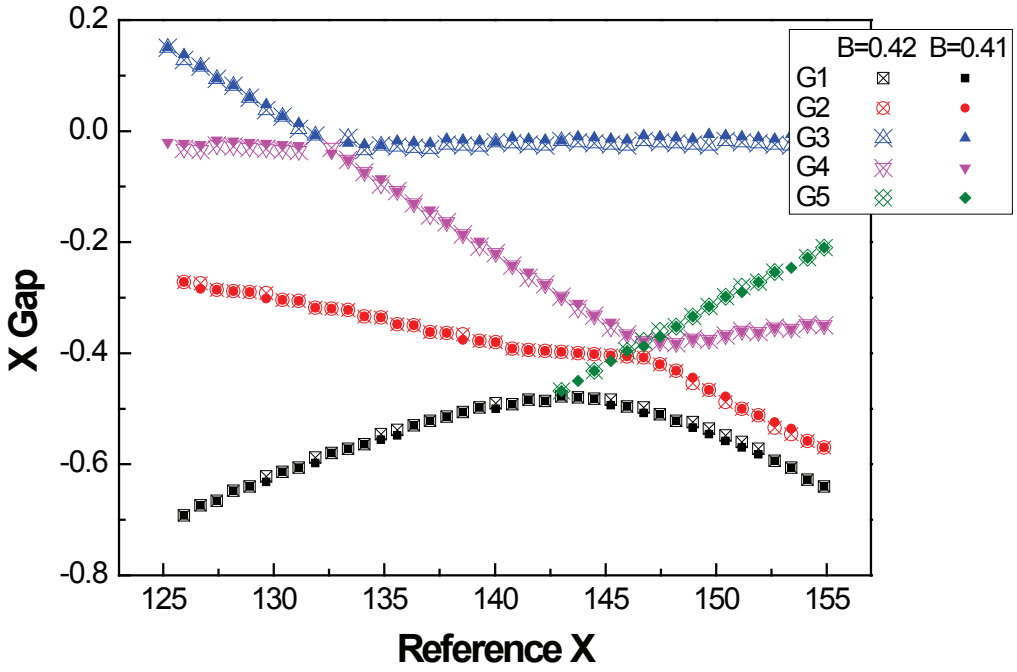

Figure 4.14: Quasi-mode evolution diagrams for $B = 0.41$ and $B = 0.42$. η for both cases are identical, 0.19.

Chapter 5

Conclusion

In this thesis, I observed several disagreement between conventional linear-approximation theory for the surface oscillation of a liquid jet and careful experimental results. It was shown that a small fraction of the boundary of an asymmetric microcavity is possible to change the internal quasi-mode dynamics seriously. The disagreements come from small perturbation($\sim 1\%$ of the mean radius) which has been neglected occasionally, especially for low-Q cavities.

Theoretically, I modified Niels Bohr's non-linear treatment for the case and derive more accurate result, and found a criterion of its relevance. In the lowest-ordered oscillation, the octapolar magnitude is approximately 0.41 times the square of the quadrupolar magnitude.

To verify this experimentally, I developed a high-resolution boundary profiling technique for an opaque two- or three-dimensional convex object with a two-fold symmetry. This technique is based on the fact that the angle width or the angular separation between two intensity minima in the

forward direction is inversely proportional to the projected width of the object in the same direction. We derived an analytic formula with which the object boundary can be reconstructed from the angle widths observed for various object rotation angles. For an object with a mean radius of 10 μm, the typical accuracy of our technique is less than 0.2% of the object size, amounting to 20 nm only. Since our technique is non-destructive and non-contact, it can be applied to determine the boundary shapes of soft matter or fluidic objects such as biological samples and liquid droplets and columns, for which the conventional techniques such as confocal scanning microscopy or other interferometry techniques are not effective.

Experimentally measured surface profiles of the liquid microjet cavities and the result of modified theoretical analysis are well agreed. By doing this, I resolved the boundary profile enough for one to analyze even sensitive quasi-mode-dynamical features. The internal quasi-modes of the liquid jet cavity are now identified in a form of $2\pi na/\lambda$ to a theoretically analyzable resonance and their dynamical behaviours are also matched well with numerical simulations. The possibility of spectroscopic analysis is one of the important advantages of the liquid microjet system, and now it can be fully appreciated. Results of this thesis are available for more detailed and precise expectations in the field of microcavity science and quantum chaos.

Appendix A

More comparison of a quadrupolar-deformed resonator with the microjet cavity

A.1 A problem of "delayed chaotic transition" of the microjet cavity compared with QDMs

A few years ago, I participated a report which contains a statement about the comparison between the PSOS structure of the resonator with the empirical boundary shape Eq. (4.1) and the quadrupolar-deformed resonator.

According to the report, if we lower the deformation parameter η of the empirical shape by 0.05∼0.08 the two PSOS structures become very similar.

Because the magnitude of the deformation parameter is strongly related to the degree of chaos in the ray dynamics, it can be understood that transition to chaos of the ray dynamics from the boundary Eq. (4.1) is delayed compared to the quadrupolar-deformed boundary with the same eccentricity. This observation gives a good qualitative method of approximation that is applicable to the semi-classical analyses. I do not intent to re-examine it here, but at this point of time, it can be questionable that then how about the quasi-mode evolution structures, instead of PSOSs.

A.2 Quasi-mode evolution diagrams for QDMs and discussions

Here I show 4 quasi-mode diagrams for quadrupolar-deformed boundaries. The eccentricity is denoted to η', instead of η to avoid confusion with the quadrupolar deformation parameter of the microjet cavity. $\eta' = 0.10$, 0.12, 0.14, and 0.16 for diagrams on Fig. A.1 to Fig. A.4, respectively.

In some cases, it is possible to find the smaller $\eta' = \eta - C$ (C is a positive constant) for a quadrupolar-deformed resonator that makes the quasi-mode evolution "similar" to that from the boundary Eq. (4.1), especially for rather small η'(upto about 0.14). However, the level of the similarity is complex.

For example, Fig. A.1 shows the quasi-mode evolution diagram for the quadrupolar-deformed resonator with $\eta' = 0.12$. The general aspects of the

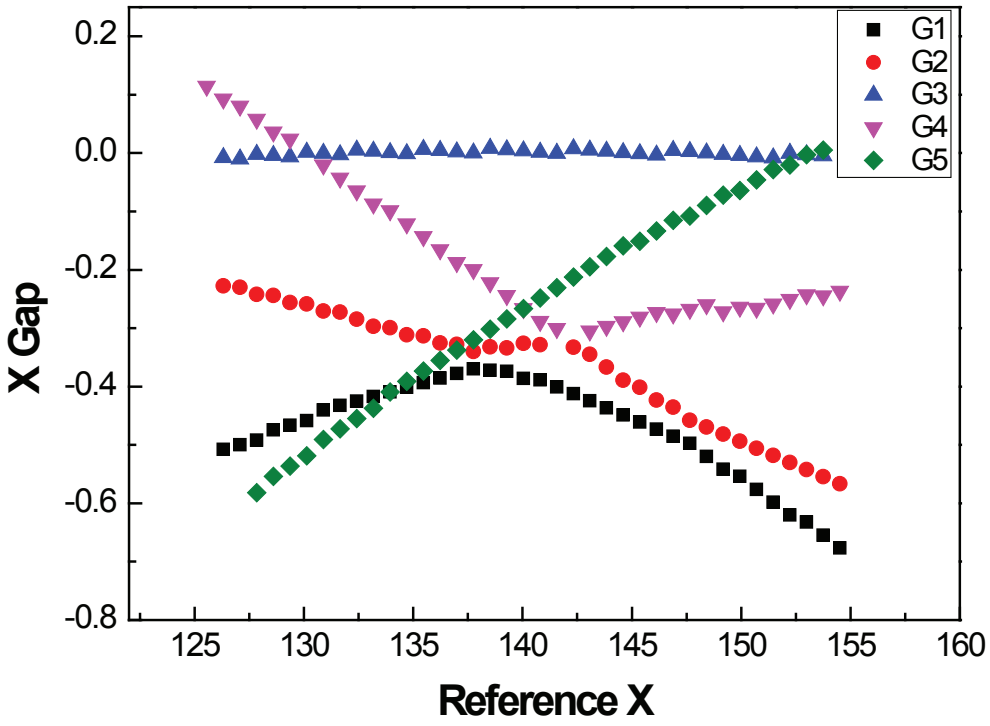

Figure A.1: The quasi-mode evolution diagram for the quadrupolar-deformed resonator with the eccentricity $\eta' = 0.10$

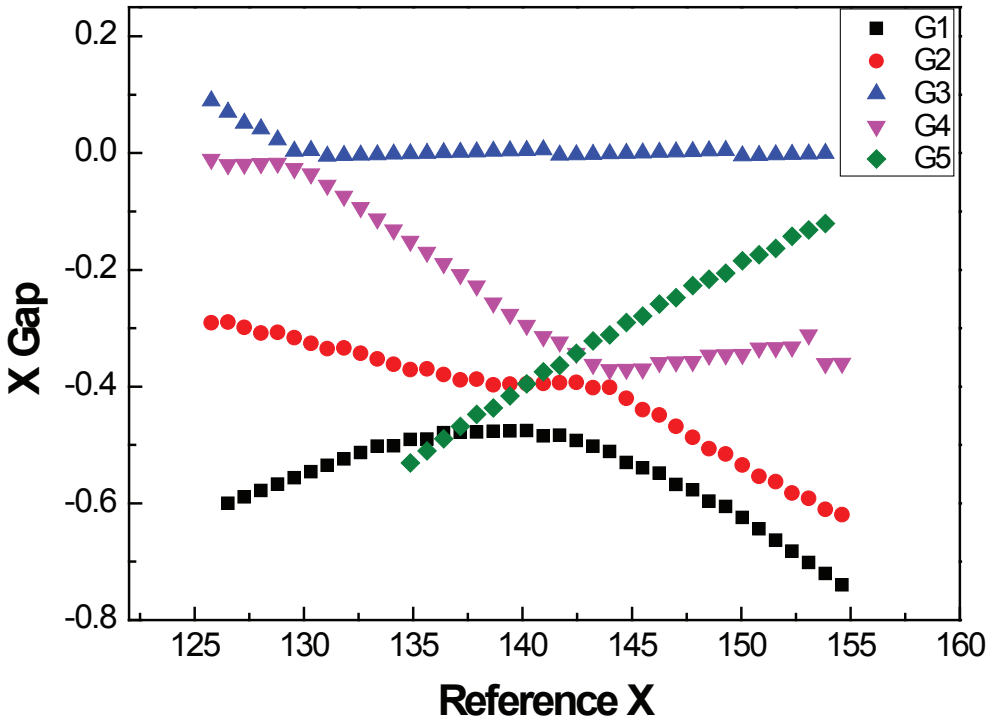

Figure A.2: The quasi-mode evolution diagram for the quadrupolar-deformed resonator with the eccentricity $\eta' = 0.12$

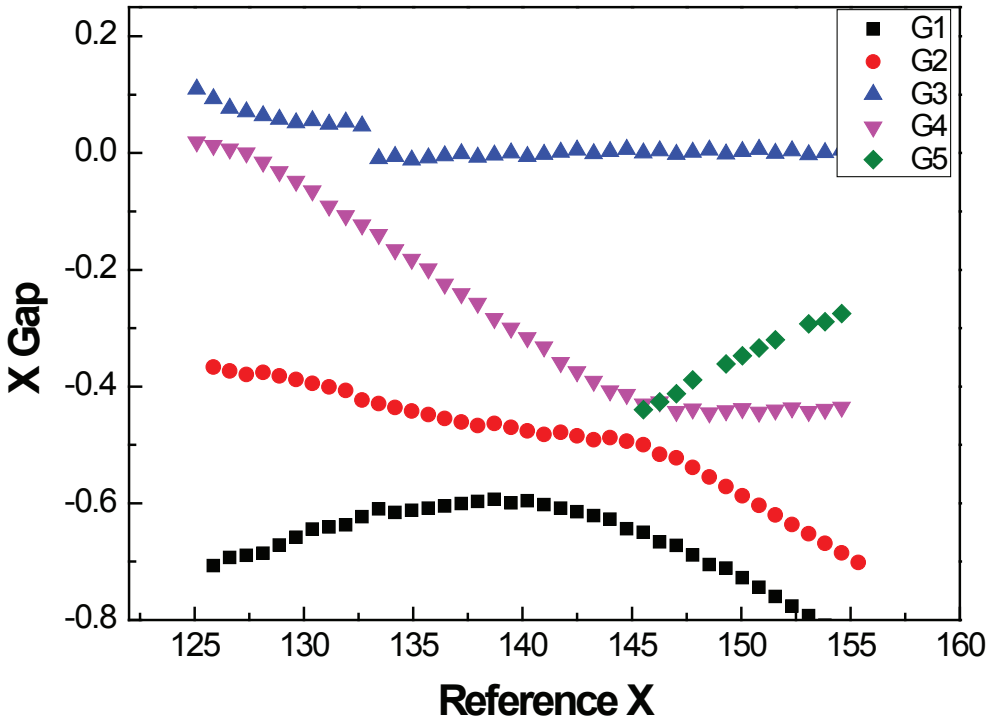

Figure A.3: The quasi-mode evolution diagram for the quadrupolar-deformed resonator with the eccentricity $\eta' = 0.14$

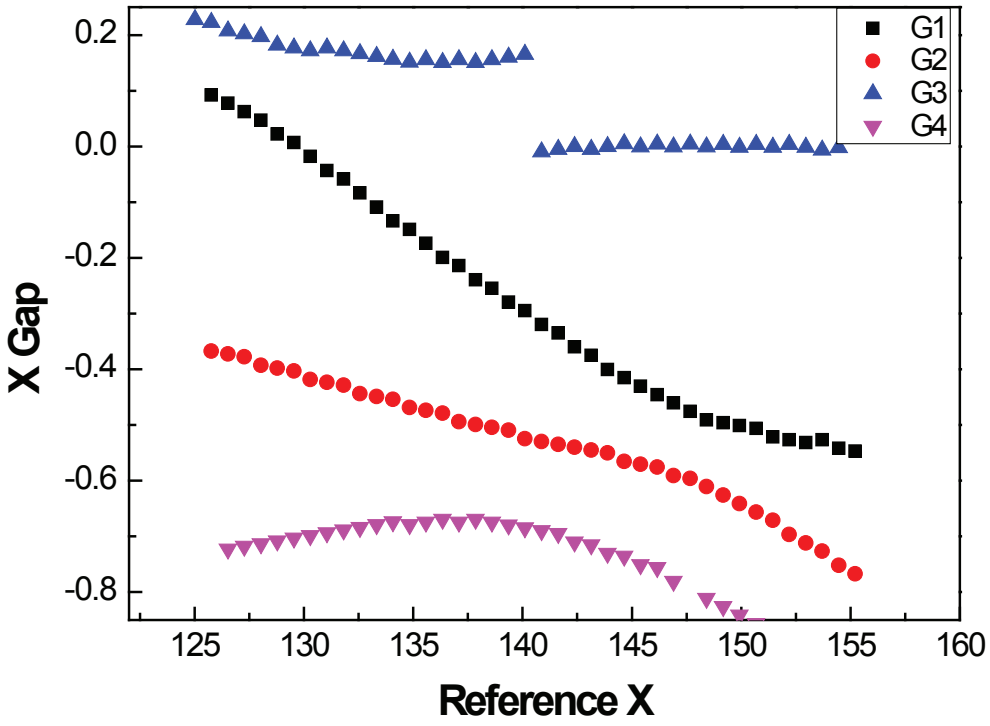

Figure A.4: The quasi-mode evolution diagram for the quadrupolar-deformed resonator with the eccentricity $\eta' = 0.16$

diagram remind the typical features I examined in this study. Namely, there exist 5 different groups, $3-4$, $1-2$, $2-4$ and again $1-2$ avoided crossing occur, and 5 penetrates other groups. However, the details make it difficult to determine what η it corresponds to. 4 covers 19 FSRs after the $3-4$ avoided crossing till avoid 2. It implies the structure is similar to that of $\eta = 0.185$. But 5 penetrates 4 two FSRs before the $2-4$ avoided crossing. In this time, it implies that $\eta{\sim}0.155$. Moreover, the second $1-2$ avoided crossing shows a considerably large gap. This strong interaction appears beyond $\eta = 0.20$. Thus it can be said that the diagram shows highly-mixed features.

It might be more striking that as shown in Fig. 2.6 at $\eta = 0.19$ the quadrupolar-deformed resonator even don't exhibits 5 quasi-mode groups. I think these examples are sufficient to show that it is dangerous to maintain the assumption of "quadrupole" for studies related to detailed quasi-mode structure.

Appendix B

On the calibration of the relative size parameter X of experimentally detected resonances

In Fig. 4.10 one can observe relatively large deviation between the experiment and the calculation compared to other examples. This is probably due to experimental error. But an overall tendency of the deviation indicates that the "error" is not a kind of random noise. It looks that the experimentally observed quasi-mode sequences are flattened ones of the corresponding theoretical curves. Is this flattening equal on all sequences? I am convinced that it is true. In Fig. B.1 a new matched diagrams are displayed. Experimental results are revised by fitting data points around the diabatic curve

between two arrows to the corresponding theoretically-obtained curve. A better agreement is now achieved. This observation indicates that this kind of error can be corrected by recalibration of the relative size parameter X.

Calibration of experimental data is an important step during the procedure to obtain a quasi-mode evolution diagram. Basically X is set to

$$X = \frac{2\pi n_0 a(1 + p\lambda + q\lambda^2)}{\lambda}, \tag{B.1}$$

where n_0 is a reference value of the index of refraction, a is the mean radius, λ is the observed wavelength, and p, q are constants. We do not know accurate conditions for $n_0 a$, p, and q thus they are fitting parameters. Various factors such as the dispersion of the index of refraction(with wavelength and temperature), mechanical vibration of the jet, and internal error of the spectrometer can vary the parameters. Sequences found out in the experiments tend to follow their respective diabatic curves. This implies that ΔXs are helpful for seeking a fit. For represented data in this thesis I assume that the visible members of the group 3 from 1.188bar-D4-20.3°C-14$\pm$1 μm CMF spectrum are regularly spaced beyond $3-4$ avoided crossing. This assumption comes from that the group 3 for η around 0.16 is relatively regular-spaced, according to calculations. This is one of the reasons why I emphasize detailed features like shown in table 4.1: to avoid a complex suspicion of logical circulation.

What is the most dominant main factor? A product of calibrated X and the observed λ yields $2\pi n_0 a f(\lambda)$, where $f(\lambda)$ is a correction function. In Fig. B.2 $f(\lambda)/f(\lambda_0)$ (λ_0 is an arbitrary origin) for the basic calibration

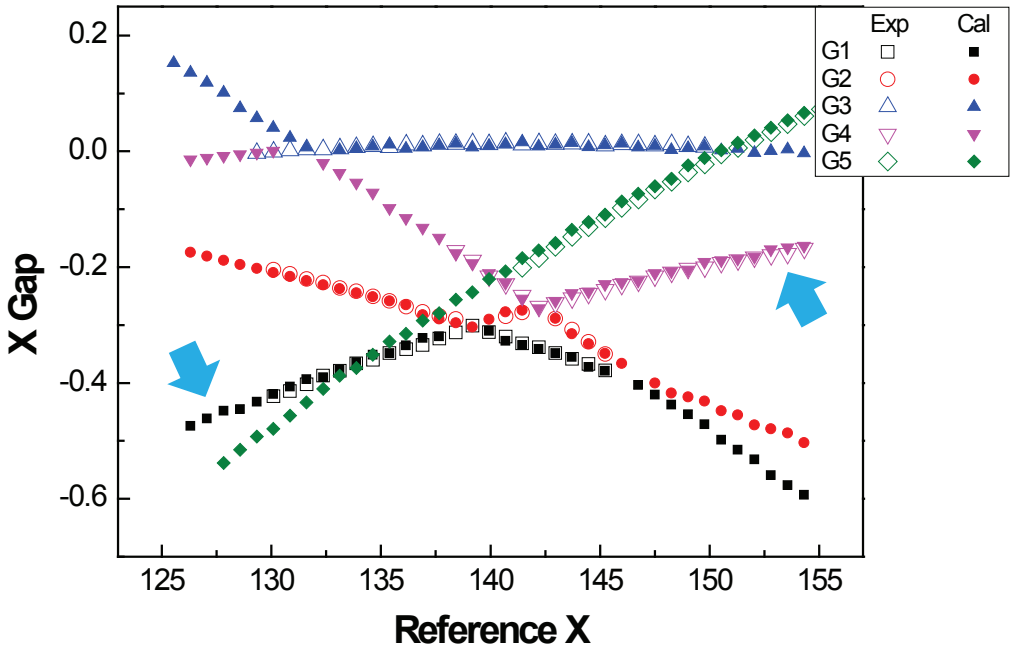

Figure B.1: A new matching for 1.326bar-D5-20.3°C. The experimental data are recalibrated. Calculated quasi-mode evolution diagram is identical to that of Fig. 4.9(a), namely, $\eta = 0.125$.

method using the group 3 for η around 0.16 is displayed. The tendency is much like that of $n(\lambda)/n(\lambda_0)$ when only its wavelength dispersion is considered and the temperature is fixed to 20.0°C. The resemblance is also observed for the special calibration that I used in this appendix to correct Fig. 4.10.

This finding shows that the most dominant factor of the calibration is the wavelength dispersion of the index of refraction. But smaller contributions that form other factors are not negligible. Change of temperature can vary n, for example. Moreover, it is noticeable that noisy tendency in Fig. B.2 is grown with the wavelength. It is probably due to the calibration of the spectrometer, because the machine I used for this study is calibrated based on one of the famous emission line of mercury lamp, 546.1nm.

Meanwhile, the calibration of Eq. (B.1) actually remains an undetermined parameter when ΔX is used as standards. If it is assumed that ΔX is known,

$$\Delta X = \Delta 2\pi n_0 a \left(\frac{1}{\lambda} + p + q\lambda\right) = \Delta 2\pi n_0 a \left(\frac{1}{\lambda} + q\lambda\right). \qquad \text{(B.2)}$$

Namely, p is still undetermined. Thus it can be happened that the calibrated diagram should be translated along the reference X-axis to seek the best match.

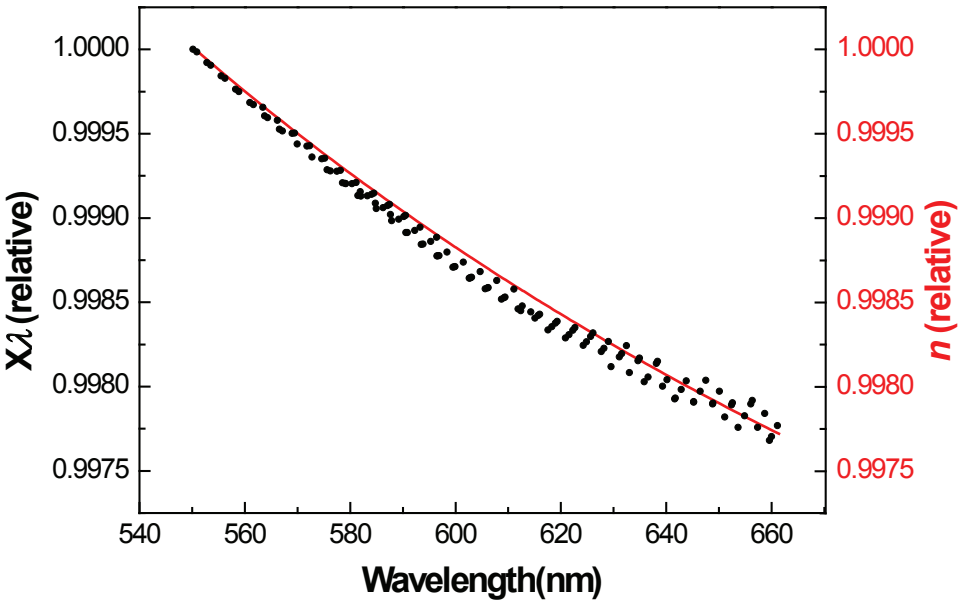

Figure B.2: Comparison between the relative values of $X\lambda$(circle) and n(line) of which wavelength dispersion is only considered.

Appendix C

On an expectation of threshold-vanishing effect of a microjet cavity laser near the exceptional point in the parametric space

The exceptional point(EP) is a point in the parametric space of a non-Hermitian Hamiltonian system where the quasi-eigenstates of this system coalesce [10]. Around the EP, it is known that a number of interesting phenomena such as exchange of quasi-eigenstates and non-trivial topology are observed. A divergent Petermann factor is one of them [59]. Petermann factor (K) [60], which is also knows as the excess noise factor of a laser [61],

can be written as following equation [62].

$$K =< \phi_n | \phi_n >, \tag{C.1}$$

where ϕ_n is the adjoint of the nth eigenmode u_n of a non-Hermitian Hamiltonian system. ϕ_n and u_n should satisfy the bi-orthogonal condition,

$$\int u_m \phi_n = \delta_{mn}. \tag{C.2}$$

For past three decades, there have been abundant controversies over the physical origin and the properties of this factor. One of the hottest debated issues is whether the Petermann factor can be interpreted as the spontaneous emission enhancement factor. Some distinguished scientists think so [62, 63, 64, 65]. But some others don't [66]. If the former opinion is right, Petermann factor can be very useful to many quantum processes [67], such as the parametric down-conversion [65]. But otherwise, it would be just a mirage.

Now, here I propose an idea of test for this issue. If the spontaneous emission is really enhanced by the Petermann factor, then the semi-classical rate equations of 2-level laser become

$$\frac{dn}{dt} = \kappa(n + K)N_2 - \kappa n N_1 - \gamma n, \tag{C.3}$$

$$\frac{dN_2}{dt} = R - \kappa n N_2 - A N_2, \tag{C.4}$$

where n is the photon number of the inspected quasi-eigenmode, κ is the coupling constant, N_2 and N_1 are populations of the excited and the ground state respectively , γ is the decay rate of the cavity, R is the pumping rate, and A is Einstein's A coefficient. Note that '1' in the original equations, which is related to the famous principle of "one spontaneous photon per one mode", is changed into K. Solving these equation at a steady state, one obtains following result.

$$n_{ss} = \frac{A}{2\kappa}\left[\left(\frac{\kappa R}{A\gamma} - 1\right) + \sqrt{\left(\frac{\kappa R}{A\gamma} - 1\right)^2 + \frac{4\kappa^2 K R}{A^2\gamma}}\right], \tag{C.5}$$

where 'ss' means steady state. Substituting A/κ (note that this quantity is the cavity mode number) to p and $\kappa R/A\gamma$ to r,

$$n_{ss} = \frac{p}{2}\left[(r-1) + \sqrt{(r-1)^2 + \frac{4Kr}{p}}\right]. \tag{C.6}$$

The result implies that the lasing threshold of the inspected mode vanishes when $K = p$. In Fig. C.1 I show curves for various K while p is set to $100,000$. That is to say, to test whether this effect is real or not, Petermann factor K should reach extremely large value that even have not been experimentally recorded yet. Now, it is noteworthy that Petermann factor diverges at the exceptional point. It was reported that the existence of an EP is discovered in the microjet cavity experiment (I, too participated in that study) [10]. The manifestation of EP to the quasi-mode evolution can be detected from that the crossing and the avoided crossing of the quasi-mode groups are exchanged at EPs. In Fig. 4.10, we observed that the

group 2 and 4 nearly coalesced near $X \sim 142$. This indicates that an EP is very close to $\eta = 0.125$ and $X = 142$ in the parametric space.

I think extensive investigation around that parameters with the microjet system is worth an effort. If the threshold-vanishing effect is observed, that would be a critical evidence of the interpretation of "spontaneous enhancement factor" for Petermann factor.

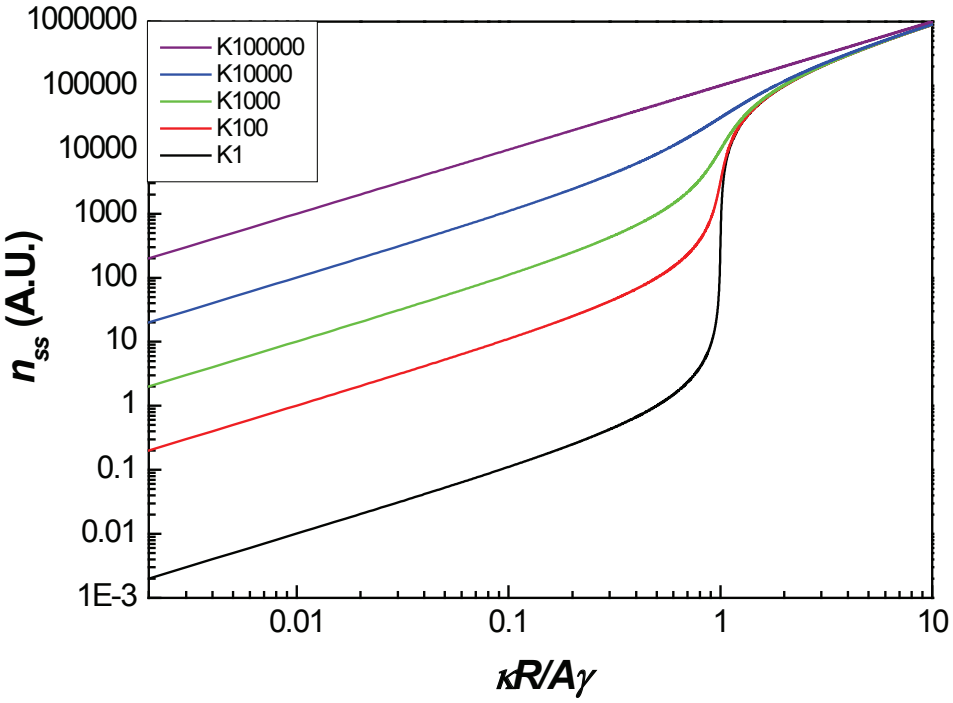

Figure C.1: Emitted photon number for various K. p is set to 100,000.

Bibliography

[1] J. U. Nöckel and A. D. Stone, Nature **385**, 45-47 (1997).

[2] C. Gmachl, F. Capasso, E. E. Narimanov, J. U. Nöckel, A. D. Stone, G. J. Faist, D. L. Sivco, and A. Y. Cho, Science **280**, 1556-1564 (1998).

[3] S. B . Lee, J.-H. Lee, J.-S. Chang, H.-J. Moon, S. W. Kim, K. An, Phys. Rev. Lett. **88**, 033903 (2002).

[4] J. Wiersig and M. Hentschel, Phys. Rev. A **73**, 031802(R) (2006).

[5] S.-B. Lee, J. Yang, S. Moon, J.-H. Lee, and K. An, J.-B. Shim, H. -W. Lee, S. W. Kim, Phys. Rev. A **75**, 011802(R) (2007).

[6] J.-B. Shim, S.-B. Lee, J. Yang, S. Moon, J.-H. Lee, K. An, H.-W. Lee, and S. W. Kim, J. Phys. Soc. Jpn. **76**, 114005 (2007).

[7] S. W. Kim, J.-B. Shim, S.-B. Lee, J. Yang, S. Moon, J.-H. Lee, K. An, and H.-W. Lee, Progress of Theoretical Physics Supplement **166**, 119 (2007).

[8] S. Shinohara, M. Hentschel, J. Wiersig, T. Sasaki, and T. Harayama, Phys. Rev. A **80**, 031801(R) (2009).

[9] Q. H. Song, L. Ge, A. D. Stone, H. Cao, J. Wiersig, J.-B. Shim, J. Unterhinninghofen, W. Fang, and G. S. Solomon, Phys. Rev. Lett. **105**, 103902 (2010).

[10] S.-B. Lee, J. Yang, S. Moon, S.-Y. Lee, J.-B Shim, S.-W. Kim, J.-H. Lee, and K. An, Phys. Rev. Lett. **103**, 134101 (2009).

[11] J. Yang, S.-B. Lee, S. Moon, S.-Y. Lee, S.-W. Kim, T. T. A. Dao, J.-H. Lee, and K. An, Phys. Rev. Lett. **104**, 243601 (2010).

[12] H. Kwak, *Observation of the resonance-assisted dynamical tunneling in a deformed microcavity.* PhD thesis, Seoul National University, 2013.

[13] A. M. Armani, R. P. Kulkami, S. E. Fraser, R. C. Flagan, and K. J. Vahala, Science **317**, 783787 (2007).

[14] J.B. Shim, S.-B. Lee, S.-W. Kim, S.-Y. Lee, J. Yang, S. Moon, J.-H. Lee, and K. An, Phys. Rev. Lett. **100**, 174102(2008).

[15] J. Yang, S. Moon, S.-B. Lee, S. W. Kim, J.-B. Shim, H.-W. Lee, J.-H. Lee, and K. An, Rev. Sci. Instrum. **77**, 083103 (2006).

[16] N. Bohr, Philos. Trans. Roy. Soc. Lond. **209** p. 281-317(1909).

[17] T. V. Kasyap, D. Sivakumar, B. N. Raghunandan, Int. J. Multiphase Flow **35**, p. 8-19(2009).

[18] Lord Rayleigh, Proc. Lond. Math. Soc. x. **4**, p. (1878).

[19] Lord Rayleigh, Roy. Soc. Proc. **29**, p. 71 (1879).

[20] Sir H. Lamb, *Hydrodynamics*(Dover Publications, New York, 1945).

[21] In general, the bottom of the jet is not a critical position. The real initial deformation is larger than that of the hole. Please see Yang(2006).

[22] Dissipation of vibration of the irrotational fluid is an ambiguous problem. In Navier-Stokes equation, the viscosity-dependent term is vanished for the potential wave. Please see an excellent review article, D. D. Joseph, International Journal of Multiphase Flow, **32**, 285-310 (2006). Bohr successively showed the linear oscillation modes have their characteristic decay rates. Meanwhile Sir. Lamb treated the problem by assuming the amplitude of vibration to be very small. The relation introduced in this thesis is basically an application of Lamb's theory to a 2-dimensional liquid volume.

[23] P. R. Berman, *Cavity Quantum Electrodynamics*(Academic Press, Boston, 1994).

[24] S.-B. Lee, J. Yang, S. Moon, S.-Y. Lee, J.-B. Shim, S.-W. Kim, J.-H. Lee, and K. An, Phys. Rev. A **80**, 011802(R) (2009).

[25] S.-B. Lee, J.-B. Shim, S. W. Kim, J. Yang, S. Moon, H.-W. Lee, J.-H. Lee, and K. An, Appl. Phys. Lett. **90**, 041106 (2007).

[26] J. Yang, S.-B. Lee, J.-B. Shim, S. Moon, S.-Y. Lee, S. W. Kim, J.-H. Lee, and K. An, Appl. Phys. Lett. **93**, 061101 (2008).

[27] J. Wiersig, J. Opt. A: Pure Appl. Opt. **5**, 53 (2003).

[28] Bohr listed 19 different surface tension coefficient values for 12°C from 71.67 dyne/cm to 77.25 dyne/cm, which were thitherto known or able to be deduced from references, while his own experimental mean was 73.23 dyne/cm. Compared with the modern value $\sim$ 73.9 dyne/cm, his result was quite good for his days.

[29] S. G. L. Harald, N. B. Rex, H. E. Tureci, R. K. Chang, A. D. Stone, T. Ben-Messaoud, and J. Zyss, J. Opt. Soc. Am. B **21**, p. 923-934 (2004).

[30] T. Tanaka, M. Hentschel, T. Fukushima, and T. Harayama, Phys. Rev. Lett. **98**, 033902 (2007).

[31] P. O. Pederson, Philos. Trans. Roy. Soc. Lond. A **207** p. 341-392(1908)

[32] The area enclosed by the profile given by Eq. 2.15 is approximately $\pi(1 + \eta^2/2)$. Therefore, to maintain the area independent of shape deformation, a correction term $-\eta^2/4$ should be present in the profile equation.

[33] Here we note that the hydrodynamic equations were treated with Poincare-Lindstedt method by J. A. Tsamopoulos et al. But we found that a few nonlinear terms were omitted in their calculation, so we do not follow their treatment. For detailed information about their study, see J. A. Tsamopoulos and R. A. Brown, J. F. Mech. **127**, pp. 519-537(1983).

[34] C. G. Rylander, D. P. Davé, T. Akkin, E. Milner, K. R. Diller, and A. J. Welch, Opt. Lett. **29**, 1509-1511 (2004).

[35] C. Joo, T. Akkin, B. Cense, B. H. Park, and J. F. de Boer, Opt. Lett. **30**, 2131-2133 (2005).

[36] W. Choi, C. Fang-Yen, K. Badizadegan, S. Oh, N. Lue, R. R. Dasari, and M. S. Feld, Nature Methods **4**, 717-719 (2007).

[37] T. Noda and S. Kawata, J. Opt. Soc. Am. A **9**, 924-931 (1992).

[38] H.-G. Döbereiner, E. Evans, M. Kraus, U. Seifert, and M. Wortis, Phys. Rev. E, **55**, 4458-4474 (1997).

[39] G. N. Constantinides, D. Gintides, S. E. Kattis, K. Kiriaki, C. A. Paraskeva, A. C. Payatakes, D. Polyzos, S. V. Tsinopoulos, and S. N. Yannopoulos, Appl. Opt. **37**, 7310-7319 (1998).

[40] Z. Chen, Appl. Opt. **45**, 6914-6918 (2006).

[41] S. V. Boriskina, P. Sewell, and T. M. Benson, J. Opt. Soc. Am. A **21**, 393-402 (2004).

[42] F. Zenhausern, Y. Martin, and H. K. Wickramasinghe, Science **269**, 1083-1085 (1995).

[43] I. Yamaguchi, J. Kato, S. Ohta, and J. Mizuno, Appl. Opt. **40**, 6177-6186 (2001).

[44] N. Lue, W. Choi, G. Popescu, T. Ikeda, R. R. Dasari, K. Badizadegan, and M. S. Feld, Appl. Opt. **46**,1836-1842 (2007).

[45] B. Bhushan, J. C. Wyant, and C. L. Koliopoulos, Appl. Opt. **24**, 1489-1497 (1985).

[46] F. Laeri and T. C. Strand, Appl. Opt. **26**, 2245-2249 (1987).

[47] M. R. Atkinson, A. E. Dixon, and S. Damaskinos, Appl. Opt. **31**, 6765-6771 (1992).

[48] H. Liang, M. G. Cid, R. G. Cucu, G. M. Dobre, A. G. Podoleanu, J. Pedro, and D. Saunders, Opt. Express **13**, 6133-6144 (2005).

[49] M. Yokota, A. Asaka, and T. Yosino, Appl. Opt. **42**, 1805-1808 (2003).

[50] S. Sonozaki, K. Iwata, and Y. Iwahashi, Appl. Opt. **42**, 6853-6858 (2003).

[51] P. Z. Takacs, E. L. Church, C. J. Bresloff, and L. Assoufid, Appl. Opt. **38**, 5468-5479 (1999).

[52] D. Narita, M. Baba, and K. Ohtani, Instrumentation and Measurement Technology Conference, IMTC '03. Proceedings of the 20th IEEE 2, 1022-1027 (2003).

[53] M. Ferraton, C. Stolz, and F. Meriaudeau, Signal-Image Technology and Internet-Based Systems. International Conference. 2008. SITIS 2008, IEEE, p. 474-479 (2008).

[54] S. Moon, J. Yang, S.-B. Lee, J.-B. Shim, S.-W. Kim, J.-H. Lee, and K. An, Optics Express **16**, 11007 (2008).

[55] M. Born and E. Wolf, *Principles of Optics: Electromagnetic Theory of Propagation, Interference and Diffraction of Light*, 7th ed. (Cambridge Univ. Press, Cambridge, 1999).

[56] J. D. Jackson, *Classical Electrodynamics*, 3rd ed. (Wiley, New York, 1998).

[57] P. M. Morse and H. Feshbach, *Methods of Theoretical Physics* (McGraw-Hill, New York, 1953).

[58] http://omlc.ogi.edu/spectra/PhotochemCAD/data/083-orig-abs.txt

[59] S.-Y. Lee, J.-W. Ryu, J.-B. Shim, S.-B. Lee, S.-W. Kim, and K. An, Phys. Rev. A **78**, 015805 (2008).

[60] K. Petermann, IEEE J. Quantum Electron. QE-15, 566-570 (1979).

[61] H. A. Haus and S. Kawakami, IEEE J. Quantum Electron. QE-21, 63-69 (1985).

[62] A. E. Siegman, Phys. Rev. A **39**, 1253-1263 (1989).

[63] A. E. Siegman, Phys. Rev. A **39**, 1264-1268 (1989).

[64] P. J. Bardroff and S. Stenholm, Phys. Rev. A **60** 2529-2533 (1999).

[65] C. Lemprecht, M. K. Olsen, M. Collett, and H. Ritsch, Phys. Rev. A **64**, 033811 (2001).

[66] I. H. Deutsch, J. C. Garrison, E. M. Wright, J. Opt. Soc. Am. B **8**, 1244-1251 (1991).

[67] A. Aiello, M. P. van Exter, G. Nienhuis, J. P. Woerdman, Optics Communications **213**, 81-87 (2002).

국 문 초 록

본 논문에서는 비투과성의 2 차원 물체가 만들어내는 회절 무늬에서 인접한 국소점들 사이의 각거리가 해당 물체의 사영 길이(projection width)와 반비례하는 규칙성이 존재한다는 점을 활용하여 기존의 정밀 측정 기술 적용이 어려웠던 액체나 부드러운 재질을 지닌 물체의 표면 형태를 복원할 수 있는 비파괴(non-destructive), 비접촉(non-contact) 측정법을 개발하고 이를 실험적으로 구현하였다. 이 측정 기술은 2 겹 대칭성(two-fold symmetry)을 갖는 물체에 적용될 수 있으며 물체 반지름의 0.2%의 분해능을 제공한다.

또한 이 측정 기술을 활용하여 반지름 약 15 마이크론의 비대칭형 미소 제트 공진기(asymmetric microjet cavity)의 표면 형태를 복원하는데 성공하였다. 그 결과 미소 액체 제트 공진기의 표면 형태는 대부분 두 개의 다중극자 성분, 즉 사중극자형(quadropolar) 진동(크기 η_1)과 팔중극자형(octapolar) 진동(크기 η_2)의 합으로 구성되어 있으며, 두 성분의 진동 크기는 $\eta_2 \approx 0.42(\pm 0.08)\,\eta_1^2$ 의 실험적인 2 차 관계식으로 연결되어 있음을 발견하였다.

액체 제트의 표면 진동에 관한 통상적인 선형 이론적 기술에 따르면 각 다중 극자형 진동 성분은 서로 독립적이다. 또한 충분한 진동 운동을 거친 뒤에는 점성(viscosity)에 의한 감쇠(dissipation) 효과로 인해 가장 낮은 차수의 운동인 사중극자형 진동이 진폭의 절대적인 대부분을 점할 것으로 예측된다. 따라서 이 실험적 결과는 선형 이론으로는 설명될 수 없다. 그러나 이는 실험 결과의 오류를 보여주는 것이 아니라, 선형 이론이 지나친 근사로 인해 지니게 된 한계를 노정한 것이다. 본 연구를 통해 발견된 2 차 관계식은 일찍이 닐스 보어(Niels Bohr)가 제시한 더욱 자세한 유체 역학적 계산과는 실험 오차의 범위 내에서 부합함을 볼 수 있었다. 본 논문에서는 닐스 보어의 계산에 그가 고려하지 않았던 제트 진행 방향 속도와 진폭에 따른 보정을 추가하였다. 2 차 관계식의 계수는 약 0.41 로 변화하지만, 여전히 실험 오차의 범위 내에서 측정 결과와 부합함을 보일 수 있었다.

미소 액체 제트 공진기는 그 재질로 인한 깨끗한 표면과, 분출 압력을 통해 그 변형도(deformation parameter)를 조절할 수 있는 장점에 힘입어 공진기 내부에

존재하는 높은 품위값(quality factor)를 갖는 속삭이는 회랑모드(whispering gallery mode)형의 준-모드(quasi-mode)의 동역학적 특성을 분광학적으로 관측할 수 있어 양자 혼돈(quantum chaos)연구의 좋은 소재로 쓰이고 있다. 그러나 그 정확한 표면 형태가 불분명함으로 인해 이론과 실험을 직접 비교하는데 지금까지는 한계가 있었다.

본 논문에서는 미소 액체 제트 공진기와 같이 높은 품위값을 가지는 공진기 시스템에서는 표면 형태의 아주 작은 차이도 내부 준-모드의 동역학적 특성을 크게 변화시킬 수 있음을 보이고, 아울러 위에서 기술한 새로운 측정 방법을 통해 얻은 결과와 보다 정밀한 유체 역학적 계산 결과로 미소 액체 제트 공진기의 표면 형태를 매우 높은 정밀도로 복원하였고, 이 형태에 대해 경계 요소법(boundary element method)을 사용한 전산 시늉 결과 도출된 이론적인 준-모드의 위치는 실험적으로 관측된 것과 실험적, 이론적 오차의 범위 내에서 거의 일치함을 확인할 수 있었다. 또한 준-모드간의 교차(crossing), 교차 회피(avoided crossing) 양상, 교차 회피 간격(avoided crossing gap) 같은 동역학적 특성들 역시 잘 예측됨을 보였다. 이러한 결과는 향후 양자 혼돈 연구와 비대칭형 유전체 미소 공진기의 준-모드 특성 연구에 공헌할 수 있을 것으로 기대된다.

주요어 : 비파괴 측정, 제트의 표면 진동, 비대칭형 미소 공진기, 분광학, 표면 형태에 민감한 준-모드, 준-모드 상호작용

학 번 : 2004 - 20395